Chaos, Solitons and Fractals 195 (2025) 116286

Contents lists available at ScienceDirect

Chaos, Solitons and Fractals

journal homepage: www.elsevier.com/locate/chaos

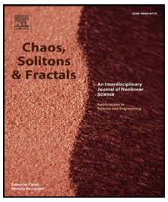

Cross-coupling in hydrodynamic phase-field models for nonisothermal binary fluids

Shouwen Sun [a], Jun Li [b], Qi Wang [c,*]

[a] School of Mathematics and Statistics, Shangqiu Normal University, Shangqiu 476000, China
[b] School of Mathematical Sciences, Tianjin Normal University, Tianjin 300387, China
[c] Department of Mathematics, University of South Carolina, Columbia, SC 29208, USA

ARTICLE INFO

Keywords:
Thermodynamical consistency
Nonisothermal binary incompressible viscous fluid flows
Cross-coupling
Entropy quadratization method
Entropy-production-rate-preserving schemes
Adaptive time-stepping

ABSTRACT

In this paper, we present a general thermodynamically consistent hydrodynamic phase-field model for nonisothermal binary viscous fluids. This model incorporates cross-coupling effects among phase, velocity and temperature, while adhering to the generalized Onsager principle and conservation laws. We systematically explore its validity across the model parameter space and provide guidelines for determining consistent, dissipative physical boundary conditions. This model preserves both fluid phase volumes and ensures positive entropy production under adiabatic and dissipative boundary conditions. We then specifically investigate the phase-temperature coupling in detail, elucidating roles played by additional reversible (nondissipative) and irreversible(dissipative) processes due to the cross-coupling. Leveraging the entropy quadratization strategy, we develop a theoretical framework for devising second-order, entropy-production-rate-preserving numerical schemes for the model. We validate the schemes through mesh refinement tests and demonstrate its efficacy using an adaptive time-stepping strategy. Four distinct phase-temperature coupling scenarios are examined to illustrate the model's capacity to capture complex interfacial dynamics in the context of Rayleigh–Bénard convection in nonisothermal binary viscous fluids. The role of cross-coupling parameters in promoting or retarding heat convection and fluid mixing via either the entropy-enhancing or entropy-preserving cross-coupling is qualitatively identified. This work advances the field by providing a robust, physically consistent framework for modeling nonisothermal binary fluid systems, with potential applications in materials science, geophysics, and engineering.

1. Introduction

Multi-component fluid flows are integral to a wide range of physical, biological, and industrial processes, including emulsions, polymer blends, multiphase flows in porous media, and atmospheric convection [1–4]. Understanding the interplay between phase separation, interfacial dynamics, and thermal effects is essential for accurately predicting and controlling these systems. Modeling such flows presents significant challenges due to the complex coupling between hydrodynamics, phase transitions, and thermodynamic constraints [5]. Traditional numerical methods, including sharp-interface tracking, volume-of-fluid approaches, and front-tracking techniques, often struggle with handling topological changes, interface coalescence, and breakup [6–9].

Phase-field models have emerged as a powerful alternative for simulating multi-component fluid flows, particularly for cases involving interfacial dynamics and phase separation [10–14]. These models represent the interface as a diffuse region, eliminating the need for explicit interface tracking while naturally incorporating thermodynamic driving forces [11,12]. Over the past two decades, phase-field methods have been widely adopted for isothermal binary and multi-component systems, with applications ranging from materials science to fluid mechanics [13–15]. However, real-world systems are rarely isothermal, temperature variations significantly impact phase transitions, diffusion processes, and hydrodynamic stability [16,17]. Despite this, much of the existing research on phase-field models has focused on isothermal conditions, leaving a critical gap in the understanding and modeling of nonisothermal multi-component fluid flows [18–22].

Several recent studies have sought to address this gap by incorporating temperature effects into phase-field models. For example, diffuse-interface models have been extended to study spinodal decomposition under thermal gradients by A. Bertei et al. [23], diffusion-interface models

---

* Corresponding author.
E-mail addresses: ssw@sqnu.edu.cn (S. Sun), nkjunli@qq.com (J. Li), qwang@math.sc.edu (Q. Wang).

https://doi.org/10.1016/j.chaos.2025.116286
Received 19 August 2024; Received in revised form 26 February 2025; Accepted 8 March 2025

was extended for numerical simulations of isothermal two-phase flows by A. Pecenko. [24], and entropy-based formulations have been proposed to ensure thermodynamic consistency in nonisothermal settings by Li et al. Guo and Lin, and our group, respectively [25–27]. In addition, Abbasi et al. and Iqbal et al. investigated entropy generation for peristaltic motion of hybrid nanofluids in a series of studies [28–30]. In solid mechanics and engineering, Long-Qing Chen reviewed the phase-field method for phase transitions/domain structures in ferroelectric thin films [31] and Indergrand et al. gave a phase-field model coupled with temperature for ferroelectric response of bulk polycrystalline PZT [32]. However, many of these approaches either neglect cross-coupling effects between phase, velocity, and temperature fields or treat them in an ad hoc manner. In reality, the interaction between thermal and phase-field dynamics is governed by fundamental principles of non-equilibrium thermodynamics, requiring a systematic derivation that ensures consistency with conservation laws and entropy production constraints [5,33–35].

In this study, we develop a general thermodynamically consistent hydrodynamic phase-field model for nonisothermal binary viscous fluids that rigorously incorporates cross-coupling effects among phase, velocity, and temperature. The model is constructed using the generalized Onsager principle, ensuring consistency with the second law of thermodynamics while capturing the intricate interplay between thermal effects and fluid dynamics. The key features of our approach include:

- Thermodynamic Consistency: The model is systematically derived to satisfy conservation laws for mass, momentum, and energy while ensuring nonnegative entropy production. This guarantees that the system remains physically meaningful under various thermal and mechanical conditions.
- Cross-Coupling Effects: Unlike previous models that treat phase and temperature evolution independently, our framework explicitly accounts for cross-coupling between phase and temperature fields. This allows for a more accurate representation of heat transfer, phase separation, and interfacial transport mechanisms.
- Boundary Conditions and Volume Conservation: We systematically explore thermodynamically consistent boundary conditions, distinguishing between adiabatic and dissipative scenarios. In particular, we identify conditions under which the volume of each fluid phase is preserved, which is crucial for maintaining physical realism in closed systems.
- Entropy Quadratization and Numerical Schemes: To develop robust and efficient computational methods, we leverage the entropy quadratization (EQ) strategy, which transforms the entropy function into a quadratic form [36–39]. This allows for the construction of second-order, entropy-production-rate-preserving numerical schemes, ensuring numerical stability and accuracy [40–42].
- Validation and Applications: The proposed model and numerical schemes are validated through mesh refinement tests and adaptive time-stepping strategies. We then apply the model to study Rayleigh–Bénard convection in nonisothermal binary fluids, demonstrating its ability to capture complex interfacial dynamics, heat-driven instabilities, and phase transitions. We analyze how different cross-coupling mechanisms influence fluid mixing, thermal convection, and interface morphology under varying parameter regimes.

Our detailed investigation of phase-temperature coupling effects reveals the existence of two distinct mechanisms that govern heat transport and fluid mixing:

1. Entropy-Enhancing (Dissipative) Coupling: This mechanism, represented by a symmetric cross-coupling mobility operator, enhances entropy production and stabilizes the system by dissipating thermal energy more efficiently. It reduces long-wavelength instabilities and promotes uniform mixing.
2. Entropy-Preserving (Reversible) Coupling: This mechanism, represented by an antisymmetric cross-coupling term in the mobility, does not contribute to entropy production but can induce dynamic instabilities. It can either enhance or retard mixing depending on its sign and magnitude, potentially leading to pattern formation and phase separation.

By systematically analyzing these mechanisms, we provide quantitative insights into the stability and dynamics of nonisothermal binary fluids, highlighting the impact of cross-coupling parameters on heat transfer and interfacial motion. Our results show that a delicate balance between entropy-enhancing and entropy-preserving processes determines the evolution of phase structure and thermal convection. The framework developed in this study offers a robust, physically consistent approach to modeling nonisothermal binary fluid systems, with potential applications across various scientific and engineering domains.

Understanding the interplay between temperature and phase separation is crucial for designing advanced materials with tailored microstructures, such as polymer blends and metallic alloys in materials science. Nonisothermal phase-field models can help simulate magma dynamics, mantle convection, and cryospheric processes where phase transitions and heat transport play a critical role in geophysics. The ability to model heat-driven multiphase flows is essential for optimizing processes in chemical engineering, energy storage, and microfluidics in engineering and industrial applications. While this study focuses on binary fluid systems, our approach can be readily extended to multi-component and quasi-incompressible fluids and solids. Future work will explore extensions to non-Newtonian fluids, various solids materials, liquid crystal polymers, and high-order numerical methods for improved computational efficiency.

The remainder of this paper is structured as follows: Section 2 presents the mathematical formulation, detailing the derivation of the governing equations in the bulk and on the boundary from the generalized Onsager principle and conservation laws. Section 3 provides a linear stability analysis, examining the impact of cross-coupling parameters on phase separation and thermal convection. Section 4 introduces structure-preserving numerical schemes, including the entropy quadratization approach and volume-preserving algorithms. Section 5 presents numerical experiments, validating the model through convergence tests and exploring phase-temperature coupling effects in Rayleigh–Bénard convection. Section 6 concludes the study by discussing the physical implications of our findings and outlines potential future research directions. By developing a rigorous and comprehensive thermodynamically consistent model, this work advances the field of multi-component fluid dynamics and opens new avenues for exploring nonisothermal phase-field phenomena.

2. Mathematical formulation

2.1. Model formulation

We formulate a general thermodynamically consistent hydrodynamic phase-field model for nonisothermal binary viscous fluids, which consists of a phase field, velocity field and temperature field, based on the generalized Onsager principle and laws of thermodynamics. The binary fluid system comprises two viscous fluid components 1 and 2, where ϕ and $\hat{\rho}_1(T)$ represent the volume fraction and the intrinsic density at temperature T of fluid 1, and $1-\phi$ and $\hat{\rho}_2(T)$ represent those of fluid 2, respectively. The overall density of the binary fluid is defined by

$$\rho(T,\phi) = \hat{\rho}_1(T)\phi + \hat{\rho}_2(T)(1-\phi). \tag{2.1}$$

If the two constituents are of equal mass densities, i.e. $\hat{\rho}_1(T) = \hat{\rho}_2(T) = \rho_0(T)$, where $\rho_0(T)$ is independent of the phase variable, $\rho = \rho_0(T)$. This is an approximation to the cases where intrinsic densities of the two fluid components are close in values. We adopt this assumption in this paper and defer the discussion of the unequal intrinsic density case to a sequel where the binary fluid is modeled as a quasi-incompressible system.

In this paper, we denote $\mathbf{v}$, e, s as the mass average velocity, the internal energy per unit volume and the entropy per unit volume, respectively. For the binary fluid system, we assume that the total entropy is given by

$$S(e,\phi,\nabla\phi) = \int_{\Omega} s(e,\phi,\nabla\phi)d\mathbf{x} = \int_{\Omega}[-\frac{\gamma_1}{2}|\nabla\phi|^2 + s_0(e,\phi)]d\mathbf{x}, \tag{2.2}$$

where Ω is the material domain that the fluid occupies, γ_1 is a parameter measuring the strength of the conformational entropy density and $s_0(e,\phi)$ is the bulk entropy density per unit volume. For the binary fluid system, we enforce laws of mass, momentum and energy conservation subject to the Boussinesq approximation [39] as follows.

Mass conservation:

$$\rho_t + \nabla\cdot(\rho\mathbf{v}) = 0. \tag{2.3}$$

In the context of the Boussinesq approximation, the above equation is approximated by

$$\nabla\cdot\mathbf{v} = 0. \tag{2.4}$$

Momentum conservation:

$$\rho[\mathbf{v}_t + \mathbf{v}\cdot\nabla\mathbf{v}] = \nabla\cdot\sigma_e - \nabla p + \mathbf{F}_e, \tag{2.5}$$

where σ_e is the extra stress tensor, p is the hydrostatic pressure and $\mathbf{F}_e$ is the extra force including the interfacial and external force [5].

Energy conservation:

$$e_t + \mathbf{v}\cdot\nabla e = (\sigma_e - p\mathbf{I}) : \nabla\mathbf{v} - \nabla\cdot\mathbf{q}, \tag{2.6}$$

where $\mathbf{q}$ is the heat flux density per unit area. Phase field variable ϕ, extra stress tensor σ_e, and heat flux $\mathbf{q}$ are additional unknowns whose transport properties need to be defined by constitutive equations [5].

Constitutive equations:

We propose that the phase field is transported by the following conservation law [11]:

$$\phi_t + \nabla\cdot(\phi\mathbf{v}) = -\nabla\cdot J, \tag{2.7}$$

where J is the excessive diffusive flux to be determined.

To derive constitutive equations for σ_e, $\mathbf{q}$ and J, we resort to the generalized Onsager principle delineated in [35]. It follows from Eqs. (2.4)–(2.7) and the fundamental relation in thermodynamics $\frac{\delta S}{\delta e} = \frac{1}{T}$ that the entropy production rate of system (2.2) is given by

$$\begin{aligned}
&\frac{dS}{dt} = \int_{\Omega}(\frac{\delta S}{\delta e}e_t + \frac{\delta S}{\delta\phi}\phi_t)d\mathbf{x} + \int_{\partial\Omega}\mathbf{n}\cdot(\frac{\partial s}{\partial\nabla\phi}\phi_t)d\mathbf{a}\\
&= \int_{\Omega}[\nabla\frac{\delta S}{\delta\phi}\cdot J + \frac{1}{T}(\sigma_e - T\frac{\partial s}{\partial\nabla\phi}\nabla\phi) : \nabla\mathbf{v} + \mathbf{q}\cdot\nabla(\frac{1}{T})]d\mathbf{x}\\
&+ \int_{\partial\Omega}\mathbf{n}\cdot[\frac{\partial s}{\partial\nabla\phi}\phi_t - (s\mathbf{I} - \frac{\partial s}{\partial\nabla\phi}\nabla\phi)\cdot\mathbf{v} - \frac{\mathbf{q}}{T} - \frac{\delta S}{\delta\phi}J]d\mathbf{a},
\end{aligned} \tag{2.8}$$

where $\mathbf{n}$ is the unit outward normal vector of $\partial\Omega$, $\frac{\delta S}{\delta\phi} = -\gamma_1\nabla^2\phi + \frac{\partial s_0}{\partial\phi}$, and equality

$$-(\frac{\delta S}{\delta e}\nabla e + \frac{\delta S}{\delta\phi}\nabla\phi)\cdot\mathbf{v} = (s\mathbf{I} - \frac{\partial s}{\partial\nabla\phi}\nabla\phi) : \nabla\mathbf{v} - \nabla\cdot[(s\mathbf{I} - \frac{\partial s}{\partial\nabla\phi}\nabla\phi)\cdot\mathbf{v}] \tag{2.9}$$

is used.

It follows from (2.8) that the entropy production rate of the system consists of two parts: the bulk entropy production rate and the entropy flux through the boundary. The bulk entropy production rate of the system is given by

$$\frac{dS_{bulk}}{dt} = \int_{\Omega}[\nabla\frac{\delta S}{\delta\phi}\cdot J + \frac{1}{T}(\sigma_e - T\frac{\partial s}{\partial\nabla\phi}\nabla\phi) : \nabla\mathbf{v} + \mathbf{q}\cdot\nabla(\frac{1}{T})]d\mathbf{x}, \tag{2.10}$$

and the entropy production rate involving the boundary or the energy flux across the boundary is defined by

$$\frac{dS_{bc}}{dt} = \int_{\partial\Omega}\mathbf{n}\cdot[\frac{\partial s}{\partial\nabla\phi}\phi_t - (s\mathbf{I} - \frac{\partial s}{\partial\nabla\phi}\nabla\phi)\cdot\mathbf{v} - \frac{\mathbf{q}}{T} - \frac{\delta S}{\delta\phi}J]d\mathbf{a}. \tag{2.11}$$

We follow the Onsager linear response theory for nonequilibrium thermodynamical systems [35] to propose the constitutive equation in the bulk as follows:

$$(J, \frac{1}{T}(\sigma_e - T\frac{\partial s}{\partial\nabla\phi}\nabla\phi), \mathbf{q})^T = \mathcal{M}\cdot(\nabla\frac{\delta S}{\delta\phi}, \mathbf{D}, \nabla\frac{1}{T})^T, \tag{2.12}$$

where $\mathcal{M} \geq 0$ is the mobility operator and $\mathbf{D}$ is the rate of strain tensor. Note that $\mathcal{M}$ is a 15×15 matrix operator if σ_e and $\mathbf{D}$ are stretched into 1×9 vectors. All vectors are represented as row vectors, second order tensors are stretched to 1×9 vectors, and fourth order tensors are represented as 81×81 second order tensors in this paper. In general, the mobility operator $\mathcal{M}(\phi,\mathbf{v},T)$ comprises a symmetric part $\mathcal{M}_s(\phi,\mathbf{v},T)$ and an antisymmetric part $\mathcal{M}_a(\phi,\mathbf{v},T)$:

$$\mathcal{M}(\phi,\mathbf{v},T) = \mathcal{M}_s(\phi,\mathbf{v},T) + \mathcal{M}_a(\phi,\mathbf{v},T). \tag{2.13}$$

Substituting (2.12) into (2.10), we arrive at

$$\begin{aligned}\frac{dS_{bulk}}{dt} &= \int_\Omega [(\nabla\frac{\delta S}{\delta\phi}, \mathbf{D}, \nabla\frac{1}{T})\cdot\mathcal{M}\cdot(\nabla\frac{\delta S}{\delta\phi}, \mathbf{D}, \nabla\frac{1}{T})^T]d\mathbf{x}\\ &= \int_\Omega [(\nabla\frac{\delta S}{\delta\phi}, \mathbf{D}, \nabla\frac{1}{T})\cdot\mathcal{M}_s\cdot(\nabla\frac{\delta S}{\delta\phi}, \mathbf{D}, \nabla\frac{1}{T})^T]d\mathbf{x}.\end{aligned} \tag{2.14}$$

In this paper, we consider a grossly simplified model whose symmetric and antisymmetric part of the mobility operator $\mathcal{M}$, respectively, are given as follows

$$\mathcal{M}_s(\phi,\mathbf{v},T) = \begin{pmatrix} M_{11} & M_{12} & M_{13}\\ M_{12} & M_{22} & M_{23}\\ M_{13} & M_{23} & M_{33}\end{pmatrix}, \quad \mathcal{M}_a(\phi,\mathbf{v},T) = \begin{pmatrix} 0 & M_{a,12} & M_{a,13}\\ -M_{a,12} & 0 & M_{a,23}\\ -M_{a,13} & -M_{a,23} & 0\end{pmatrix} \tag{2.15}$$

where $M_{ij}, M_{a,ij}, i,j=1,2,3$ are entries in the mobility operator, $M_{ij}, M_{a,ij}, i\neq j$ represent the cross-coupling effects between the phase and velocity field, phase and temperature field, velocity and temperature field, respectively. They are tensors ranked from the second order up to the fourth order. The inner product between vectors is denoted by $(\bullet)$ and that between second order tensors or stretched 9×1 vectors by $(:)$. With these, the bulk entropy production rate is given by

$$\begin{aligned}\frac{dS_{bulk}}{dt} &= \int_\Omega(\nabla\frac{\delta S}{\delta\phi}\cdot M_{11}\cdot\nabla\frac{\delta S}{\delta\phi} + \mathbf{D} : M_{22} : \mathbf{D} + \nabla\frac{1}{T}\cdot M_{33}\cdot\nabla\frac{1}{T}\\ &+2\nabla\frac{\delta S}{\delta\phi}\cdot M_{12} : \mathbf{D} + 2\mathbf{D} : M_{23}\cdot\nabla\frac{1}{T} + 2\nabla\frac{\delta S}{\delta\phi}\cdot M_{13}\cdot\nabla\frac{1}{T})d\mathbf{x}\geq 0.\end{aligned} \tag{2.16}$$

Here, the semi-positive definiteness of $\mathcal{M}_s\geq 0$ warrants a positive entropy production rate and thereby thermodynamical consistency.

It follows from (2.12) and (2.15) that the constitutive equations are given by

$$\begin{cases} J = M_{11}\cdot\nabla\frac{\delta S}{\delta\phi} + (M_{12}+M_{a,12}) : \mathbf{D} + (M_{13}+M_{a,13})\cdot\nabla\frac{1}{T},\\ \sigma_e = -\gamma_1 T\nabla\phi\otimes\nabla\phi + (M_{12}-M_{a,12})\cdot T\nabla\frac{\delta S}{\delta\phi} + M_{22} : T\mathbf{D} + (M_{23}+M_{a,23})\cdot T\nabla\frac{1}{T},\\ \mathbf{q} = (M_{13}-M_{a,13})\cdot\nabla\frac{\delta S}{\delta\phi} + (M_{23}-M_{a,23}) : \mathbf{D} + M_{33}\cdot\nabla\frac{1}{T}.\end{cases} \tag{2.17}$$

In this paper, the internal energy density is approximated by

$$e = C_A T, \tag{2.18}$$

where C_A is a constant specific heat [27], and the bulk entropy by

$$s_0 = C_A(\ln T - \ln T_M) - F(\phi,T) + C_A, \tag{2.19}$$

where $F(\phi,T)$ a double well potential function of two local minima 0 and 1, respectively.

The corresponding general governing system of equations in the bulk is summarized below

$$\begin{cases}\phi_t + \nabla\cdot(\phi\mathbf{v}) = -\nabla\cdot(M_{11}\cdot\nabla\frac{\delta S}{\delta\phi} + (M_{12}+M_{a,12}) : \mathbf{D} + (M_{13}+M_{a,13})\cdot\nabla\frac{1}{T}),\\ \nabla\cdot\mathbf{v} = 0,\\ \rho(\mathbf{v}_t + \mathbf{v}\cdot\nabla\mathbf{v}) = \nabla\cdot\sigma_e - \nabla p + \mathbf{F}_e,\\ \sigma_e = -\gamma_1 T\nabla\phi\otimes\nabla\phi + (M_{12}-M_{a,12})\cdot T\nabla\frac{\delta S}{\delta\phi} + M_{22} : T\mathbf{D} + (M_{23}+M_{a,23})\cdot T\nabla\frac{1}{T},\\ e_t + \mathbf{v}\cdot\nabla e = \sigma_e : \nabla\mathbf{v} - \nabla\cdot((M_{13}-M_{a,13})\cdot\nabla\frac{\delta S}{\delta\phi} + (M_{23}-M_{a,23}) : \mathbf{D} + M_{33}\cdot\nabla\frac{1}{T}),\\ e = C_A T, \quad S = -\frac{\gamma_1}{2}\|\nabla\phi\|^2 + s_0(e,\phi), \quad s_0 = C_A(\ln T - \ln T_M) - F(\phi,T) + C_A,\end{cases} \tag{2.20}$$

where T_M is a critical temperature. This completes the formulation of the general thermodynamically consistent binary fluid model in the bulk.

If we denote the volume of fluid 1 as $V = \int_\Omega \phi d\mathbf{x}$, it follows from ((2.20)-1) that

$$\frac{dV}{dt} = \int_\Omega \phi_t d\mathbf{x} = -\int_{\partial\Omega}\mathbf{n}\cdot(M_{11}\cdot\nabla\frac{\delta S}{\delta\phi} + (M_{12}+M_{a,12}) : \mathbf{D} + (M_{13}+M_{a,13})\cdot\nabla\frac{1}{T} + \phi\mathbf{v})d\mathbf{a}. \tag{2.21}$$

This serves as a physical constraint for the model. If the volume of fluid 1 is conserved ($\frac{dV}{dt}=0$) in a closed system, proper boundary conditions have to be prescribed along the boundary of the domain consistent with the volume-preserving constraint.

In this study, we focus on the phase-temperature coupling effect by examining a special case of the model, where mobility operator $\mathcal{M}(\phi,\mathbf{v},T)$ is one of a special form with cross-coupling between the phase field and the temperature field given as follows

$$\mathcal{M}(\phi,\mathbf{v},T) = \begin{pmatrix} M\mathbf{I} & 0 & (M_{13}+M_{a,13})\mathbf{I}\\ 0 & 2\eta(T,\phi)\mathbf{II} & 0\\ (M_{13}-M_{a,13})\mathbf{I} & 0 & D_0T^2\mathbf{I}\end{pmatrix}, \tag{2.22}$$

where the parameters are assumed constants, $\mathbf{I} = (\delta_{ij})_{3\times 3}$ and $\mathbf{II}$ is the fourth order identity tensor. In particular, we choose

$$\eta(T,\phi) = \frac{\eta_0^{(1)}}{T}e^{(\frac{E_a^{(1)}}{RT})}\phi + \frac{\eta_0^{(2)}}{T}e^{(\frac{E_a^{(2)}}{RT})}(1-\phi), \tag{2.23}$$

where $\eta_0^{(i)}, E_a^{(i)}, R, i=1,2$ are constants [43]. The semi-positive definiteness of the symmetric operator is warranted provided

$$M\geq 0,\ \eta\geq 0,\ D_0\geq 0,\ MD_0 + \frac{M_{a,13}^2}{T^2} - \frac{M_{13}^2}{T^2}\geq 0. \tag{2.24}$$

These impose a constraint on model parameter M_{13} as follows

$$M_{13}^2 \leq MD_0T^2 + M_{a,13}^2. \tag{2.25}$$

Notice that there is no constraint on $M_{a,13}$ though. This indicates that cross-coupling parameter M_{13} cannot be too large for the model to be thermodynamically consistent.

The governing system of equations of the simplified non-isothermal hydrodynamic model is given by

$$\begin{cases} \phi_t + \nabla \cdot (\phi \mathbf{v}) = -\nabla \cdot (M \nabla \frac{\delta S}{\delta \phi} + (M_{13} + M_{a,13}) \nabla \frac{1}{T}), \\ \nabla \cdot \mathbf{v} = 0, \\ \rho(\mathbf{v}_t + \mathbf{v} \cdot \nabla \mathbf{v}) = \nabla \cdot \sigma_e - \nabla p + \mathbf{F}_e, \\ \sigma_e = -\gamma_1 T \nabla \phi \otimes \nabla \phi + 2\eta : T\mathbf{D}, \\ e_t + \mathbf{v} \cdot \nabla e = \sigma_e : \nabla \mathbf{v} - \nabla \cdot ((M_{13} - M_{a,13}) \nabla \frac{\delta S}{\delta \phi} + D_0 T^2 \nabla \frac{1}{T}). \end{cases} \tag{2.26}$$

The corresponding non-negative bulk entropy production rate of this model is given by

$$\frac{dS_{bulk}}{dt} = \int_\Omega (\mathbf{M} |\nabla \frac{\delta S}{\delta \phi}|^2 + 2\eta \mathbf{D} : \mathbf{D} + \frac{D_0}{T^2} |\nabla T|^2 + 2M_{13} \nabla \frac{\delta S}{\delta \phi} \nabla \frac{1}{T}) d\mathbf{x} \geq 0. \tag{2.27}$$

To amplify the roles played by the symmetric and antisymmetric component to the cross-coupling effect, we investigate four limiting cases of the model in the rest of the paper in details.

- Model 1: $M_{13} = M_{a,13} = 0$. This model does not have cross-coupling which was studied in [27] previously.
- Model 2: $M_{a,13} = 0$. This model has cross-coupling though a dissipative mechanism with a constraint on model parameter M_{13} by Eq. (2.25).
- Model 3: $M_{13} = 0$. This model implements cross-coupling through a reversible transport mechanism so as to the cross-coupling effect does not impact the entropy production rate.
- Model 4: the general model with $M_{13}, M_{a,13} \neq 0$. This model implements cross-coupling via both dissipative and reversible mechanism with a constraint on model parameter M_{13} by Eq. (2.25).

We next present some sufficient physical boundary conditions for a positive entropy gain through $\partial\Omega$ for the general model.

2.2. Physical boundary conditions for entropy gains

We note that any physical boundary conditions should be determined in consultation with the entropy production rate involving the boundary or the entropy flux through the boundary, $\frac{dS_{bc}}{dt}$, given by (2.11). For clarity, we express it as an inner product below

$$\frac{dS_{bc}}{dt} = \int_{\partial\Omega} (\mathbf{n} \cdot \frac{\partial s}{\partial \nabla \phi}, -\mathbf{n} \cdot (s\mathbf{I} - \frac{\partial s}{\partial \nabla \phi} \nabla \phi), -\frac{1}{T}, -\frac{\delta S}{\delta \phi}) \cdot (\phi_t, \mathbf{v}, \mathbf{n} \cdot \mathbf{q}, \mathbf{n} \cdot J)^T d\mathbf{a}. \tag{2.28}$$

For a dissipative system, we assume that the entropy flux contributes a positive contribution to the total entropy production in Ω. This is a tricky issue which entails two scenarios: 1. the entropy flux across the boundary is nonnegative everywhere, 2. the net entropy flux across the boundary is nonnegative, which allows the entropy flux to be nonnegative at some places along the boundary while negative at other places, but the net flux across the boundary is nonnegative. In the following, we present boundary conditions consistent with scenario 1.

Applying the general Onsager principle to entropy flux in case 1, we obtain

$$(\phi_t, \mathbf{v}, \mathbf{n} \cdot \mathbf{q}, \mathbf{n} \cdot J)^T = \mathcal{M}_b \cdot (\mathbf{n} \cdot \frac{\partial s}{\partial \nabla \phi}, -\mathbf{n} \cdot (s\mathbf{I} - \frac{\partial s}{\partial \nabla \phi} \nabla \phi), -\frac{1}{T}, -\frac{\delta S}{\delta \phi})^T, \tag{2.29}$$

where $\mathcal{M}_b$ is the boundary mobility operator, a 6×6 matrix operator. If $\mathcal{M}_b \geq 0$, this boundary condition provides a sufficient condition that warrants a positive contribution to the total entropy production rate from the boundary terms everywhere. It is thus termed dissipative boundary condition [44,45]. This boundary condition family is natural and physical. However, in cases besides case 1 and 2, the boundary condition affected by external means may yield a negative entropy flux despite that the bulk entropy production rate is positive. If the entropy flux at the boundary does not contribute a positive influx, the system could not be guaranteed a dissipative system definitively.

From (2.11), we identify a host of entropy fluxes across $\partial\Omega$ associated with different physical mechanisms:

- $\mathbf{n} \cdot \frac{\partial s}{\partial \nabla \phi} \phi_t$ is the entropy flux density due to the volume fraction flux;
- $-\mathbf{n} \cdot [\mathbf{v} \cdot (s\mathbf{I} - \frac{\partial s}{\partial \nabla \phi} \nabla \phi)]$ is the entropy flux due to the convective normal velocity;
- $-\mathbf{n} \cdot \frac{\mathbf{q}}{T}$ is the excessive entropy flux density due to the heat;
- $-\mathbf{n} \cdot [J \frac{\delta S}{\delta \phi}]$ is the entropy flux due to the excessive volume fraction flux.

These fluxes play distinctive roles in determining the physical boundary conditions of the model.

Adiabatic boundary conditions: A set of sufficient physical boundary conditions corresponding to zero entropy fluxes at the boundary are known as the adiabatic boundary conditions, given by

$$\mathbf{n} \cdot \nabla \phi |_{\partial\Omega} = 0, \quad \mathbf{v} |_{\partial\Omega} = 0, \quad \mathbf{n} \cdot \nabla \frac{\delta S}{\delta \phi} |_{\partial\Omega} = 0, \quad \mathbf{n} \cdot \nabla T |_{\partial\Omega} = 0; \tag{2.30}$$

or equivalently,

$$\frac{\partial s}{\partial \nabla \phi} \cdot \mathbf{n} |_{\partial\Omega} = 0, \quad \mathbf{v} |_{\partial\Omega} = 0, \quad J \cdot \mathbf{n} |_{\partial\Omega} = 0, \quad \mathbf{n} \cdot \mathbf{q} |_{\partial\Omega} = 0. \tag{2.31}$$

These boundary conditions make $\frac{dS_{bc}}{dt} = 0$. Then, it follows from $\frac{dS}{dt} = \frac{dS_{bulk}}{dt} \geq 0$, which indicates that the bulk equations coupled with the adiabatic BCs yield a positive entropy production rate. In addition, these boundary conditions warrants $\frac{dV}{dt} = 0$ so that the volume of fluid 1 phase is conserved.

Dissipative boundary conditions: If there are entropy exchanges between the interior of the domain and the surrounding in such a way that the net entropy influx is positive, we have the non-adiabatic boundary conditions given by (2.29). There could be infinitely many such conditions in this class. For example, all boundary conditions given by (2.29) are in this class so long as $\mathcal{M}_b \geq 0$.

Physically nonadiabatic boundary conditions: Other type boundary conditions may be applicable in the real-world when there are nontrivial boundary fluxes sustained by an adjacent reservoir. For example, we consider the phenomenon of Rayleigh–Bénard convection in the nonisothermal binary fluid flow, in which the temperature is prescribed along a portion of the boundary. It inevitably creates entropy fluxes crossing boundaries of the physical domain that the binary fluid occupies. For example, the following physical boundary conditions are usually used for this problem:

$$\mathbf{n}\cdot\nabla\phi\mid_{\partial\Omega}=0,\quad \mathbf{v}\mid_{\partial\Omega}=0,\quad \mathbf{n}\cdot\nabla\frac{\delta S}{\delta\phi}\mid_{\partial\Omega}=0,\quad \mathbf{n}\cdot\nabla T\mid_{\partial\Omega_1}\neq 0,\quad T|_{\partial\Omega_2}=T_b(\mathbf{x}), \tag{2.32}$$

where $\partial\Omega_1$ and $\partial\Omega_2$ are two disjoint boundaries of Ω with $\partial\Omega_1+\partial\Omega_2=\partial\Omega$ and $T_b>0$ is a prescribed temperature along $\partial\Omega_2$. These boundary conditions produce a boundary entropy flux that is indefinite in general. The overall entropy production of the system in Ω can thus be indefinite.

We remark that a thermodynamically consistent model is determined by its bulk entropy production property together with proper boundary conditions. In a bounded domain, boundary conditions contribute additional entropy fluxes which can be instrumental in the thermodynamical consistency of the model. If the boundary fluxes contribute a positive entropy flux, the model together with the boundary conditions is thermodynamically consistent. Even if the boundary flux is indefinite but the bulk entropy production dominates, we expect our numerical approximations would respect the boundary flux thereby the overall physical property of the model.

2.3. Non-dimensionalization

Using characteristic length scale L, temperature scale ΔT, density scale ρ_0 and velocity scale U, we obtain the corresponding dimensionless parameters and the physical variables as follows:

$$\begin{aligned}
&\phi=\hat{\phi},\quad \mathbf{x}=\hat{\mathbf{x}}L,\quad \mathbf{v}=\hat{\mathbf{v}}U,\quad t=\hat{t}\frac{L}{U},\quad T=\hat{T}\Delta T,\quad \rho=\hat{\rho}\rho_0,\quad M=\hat{M}\frac{\Delta T L}{\rho_0 U},\\
&\frac{\delta S}{\delta\phi}=\frac{\delta\hat{S}}{\delta\phi}\frac{\rho_0U^2}{\Delta T},\quad M_{13}=\hat{M}_{13}\Delta T LU,\quad M_{a,13}=\hat{M}_{a,13}\Delta T LU,\quad \sigma_e=\hat{\sigma}_e\rho_0U^2,\\
&p=\hat{p}\rho_0U^2,\quad \mathbf{F}_e=\hat{\mathbf{F}}_e\frac{\rho_0U^2}{L},\quad \gamma_1=\hat{\gamma}_1\frac{\rho_0U^2L^2}{\Delta T},\quad \eta=\hat{\eta}\frac{\rho_0UL}{\Delta T},\quad e=\hat{e}\rho_0U^2,\\
&C_A=\hat{C}_A\frac{\rho_0U^2}{\Delta T},\quad s_0=\hat{s}_0\frac{\rho_0U^2}{\Delta T},\quad S=\hat{S}\frac{\rho_0U^2L^2}{\Delta T}\quad D_0=\hat{D}_0\frac{\rho_0LU^3}{\Delta T}.
\end{aligned} \tag{2.33}$$

The dimensionless equations without the ̂s are given below.

$$\begin{cases}
\phi_t+\nabla\cdot(\phi\mathbf{v})=-\nabla\cdot(M\nabla\frac{\delta S}{\delta\phi}+(M_{13}+M_{a,13})\nabla\frac{1}{T}),\\
\nabla\cdot\mathbf{v}=0,\\
\rho(\mathbf{v}_t+\mathbf{v}\cdot\nabla\mathbf{v})=\nabla\cdot\sigma_e-\nabla p+\mathbf{F}_e,\\
\sigma_e=-\gamma_1T\nabla\phi\otimes\nabla\phi+2\eta:T\mathbf{D},\\
e_t+\mathbf{v}\cdot\nabla e=\sigma_e:\nabla\mathbf{v}-\nabla\cdot((M_{13}-M_{a,13})\nabla\frac{\delta S}{\delta\phi}+D_0T^2\nabla\frac{1}{T}),\\
e=C_AT,\quad S=-\frac{\gamma_1}{2}\|\nabla\phi\|^2+s_0(e,\phi),\quad s_0=C_A(\ln T-\ln T_M)-F(\phi,T)+C_A.
\end{cases} \tag{2.34}$$

Next, we examine the near equilibrium dynamics of Model 4 to highlight the role played by the phase-temperature coupling parameter M_{13} and $M_{a,13}$.

3. Near equilibrium dynamics

We examine near equilibrium dynamics of Model 4, through a linear analysis about a constant equilibrium state: $\phi=\phi_0,\mathbf{v}=\mathbf{0},T=T_0$, where $\phi_0\in[0,1]$ and $T_0>0$ are constants. We adopt a specific double well potential given by

$$F(\phi,T)=\gamma_2(T)\phi^2(1-\phi^2), \tag{3.1}$$

where γ_2 measures the strength of the bulk repulsive potential. We denote

$$F_1(\phi,T)=F'(\phi)=2\gamma_2(T)\phi(1-\phi)(1-2\phi),\quad F_2(\phi,T)=F''(\phi)=2\gamma_2(T)(6\phi^2-6\phi+1). \tag{3.2}$$

Consider a perturbation of $\phi,\mathbf{v},T$ about their constant states $\phi=\phi_0,\mathbf{v}=\mathbf{0},T=T_0$ as follows

$$\phi=\phi_0+\varepsilon\delta\phi,\ \mathbf{v}=0+\varepsilon\delta\mathbf{v},\ T=T_0+\varepsilon\delta T. \tag{3.3}$$

The linearized equations of (2.34) in the limiting case of Model 4 reduce to the following coupled equations

$$\begin{cases}
\delta\phi_t=-\nabla\cdot\left[M(\nabla(\gamma_1\Delta\delta\phi)-F_2(\phi_0,T_0)\nabla\delta\phi)-\frac{M_{13}+M_{a,13}}{T_0^2}\nabla\delta T\right],\\
C_A\delta T_t=-\nabla\cdot\left[(M_{13}-M_{a,13})(\nabla(\gamma_1\Delta\delta\phi)-F_2(\phi_0,T_0)\nabla\delta\phi)-D_0\nabla\delta T\right].
\end{cases} \tag{3.4}$$

together with the decoupled, linearized momentum equation that contributes to some viscosity-induced decay modes.

The dispersion equation of (3.4) is given by

$$\begin{vmatrix}
\alpha+M\mathbf{k}^2\beta & \frac{(M_{13}+M_{a,13})\mathbf{k}^2}{T_0^2}\\
(M_{13}-M_{a,13})\mathbf{k}^2\beta & C_A\alpha+D_0\mathbf{k}^2
\end{vmatrix}=0, \tag{3.5}$$

where $\beta=\gamma_1\mathbf{k}^2+F_2(\phi_0,T_0)$. Growth rate α is a root of the following quadratic algebraic equation,

$$C_A\alpha^2+(D_0+C_AM\beta)\mathbf{k}^2\alpha+(MD_0-\frac{M_{13}^2-M_{a,13}^2}{T_0^2})\beta\mathbf{k}^4=0. \tag{3.6}$$

Its two roots are

$$\begin{cases}
\alpha_1=-\frac{\mathbf{k}^2}{2C_A}\left[(D_0+C_AM\beta)-\sqrt{\Delta_\alpha}\right]=-2\frac{\mathbf{k}^2\beta}{T_0^2}\left[\frac{MD_0T_0^2+M_{a,13}^2-M_{13}^2}{(D_0+C_AM\beta)+\sqrt{\Delta_\alpha}}\right],\\
\alpha_2=-\frac{\mathbf{k}^2}{2C_A}\left[(D_0+C_AM\beta)+\sqrt{\Delta_\alpha}\right],
\end{cases} \tag{3.7}$$

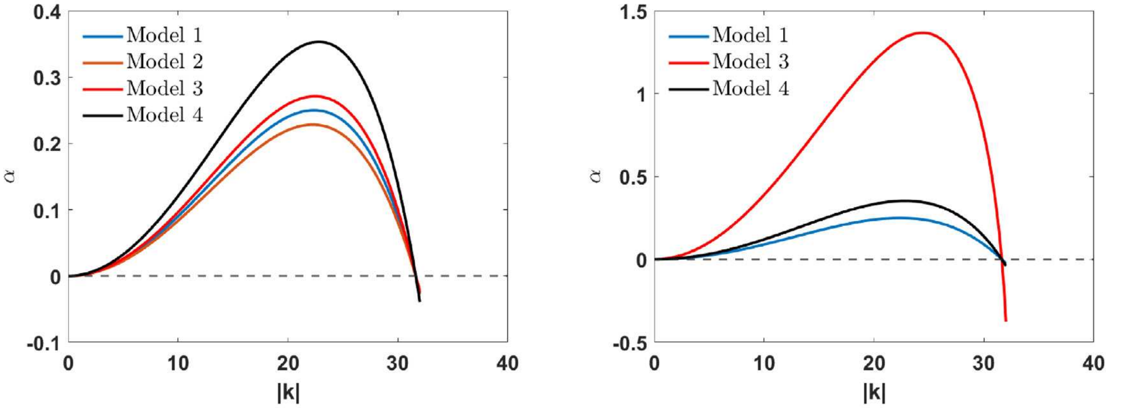

(a) Comparison of growth rates for the four models. (b) Comparison of growth rates under $M_{a,13} = 10^{-2}$

Fig. 3.1. The positive growth rate (α_1) of the four models. (a). The growth rate of the four models at different values of $(M_{13}, M_{a,13})$. Model 1: $M_{13} = 0$, $M_{a,13} = 0$, Model 2: $M_{13} = 10^{-3}$, $M_{a,13} = 0$, Model 3: $M_{13} = 0$, $M_{a,13} = 10^{-3}$, and Model 4: $M_{13} = 10^{-3}$, $M_{a,13} = 2.5 \times 10^{-3}$. The growth rate of Model 3 is greater than that of Model 1, the growth rate of Model 1 is greater than that of Model 2, but all are smaller than that of Model 4. (b) The growth rate of models 1, 3, and 4. The parameters of Model 1 and 4 are the same as those in (a) while $M_{a,13}$ in Model 3 increases 10^{-3} to 10^{-2}. The result shows that the growth rate of Model 3 increases significantly, which is much higher than that of Model 1 and Model 4. These results highlight the stabilizing effect of M_{13} and destabilizing effect of $M_{a,13}$ when the model is well-posed.

where

$$\begin{aligned} \Delta_\alpha &= (D_0 - C_A M\beta)^2 + 4C_A \frac{M_{13}^2 - M_{a,13}^2}{T_0^2}\beta \\ &= (D_0 + C_A M\beta)^2 - \tfrac{4C_A\beta}{T_0^2}(D_0 M T_0^2 + M_{1,13}^2 - M_{13}^2). \end{aligned} \tag{3.8}$$

If the model is well-posed, i.e., $M_{13}^2 - M_{a,13}^2 \le M D_0 T_0^2$, and $\beta \le 0$,

$$\Delta_\alpha = (D_0 - C_A M\beta)^2 + 4C_A \frac{M_{13}^2 - M_{a,13}^2}{T_0^2}\beta \ge (D_0 - C_A M\beta)^2 + 4C_A M D_0\beta = (D_0 + C_A M\beta)^2. \tag{3.9}$$

Then,

$$(D_0 + C_A M\beta) + \sqrt{\Delta_\alpha} \ge (D_0 + C_A M\beta) + |(D_0 + C_A M\beta)| = \max(0, 2D_0 + C_A M\beta) \ge 0. \tag{3.10}$$

This implies $Re(\alpha_2) \le 0$. On the other hand, if $\beta \ge 0$, then $Re(\alpha_2) < 0$. So, regardless of the sign of β, $Re(\alpha_2) \le 0$. This indicates that the second mode associated with α_2 is always non-positive for any wave number regardless of the sign of β.

The sign of α_1 depends on the sign and magnitude of β. In some parameter regime, $Re(\alpha_1) > 0$ for wave number $\mathbf{k}$ in the long wave range. The cutoff wave number for the instability is given by

$$\|\mathbf{k}\|_{\text{cutoff}} = \sqrt{-\frac{F_2(\phi_0, T_0)}{\gamma_1}}. \tag{3.11}$$

This simple analysis reveals that the range of instability is completely determined by the balance between the bulk free energy and the conformational entropy at steady state ϕ_0, independent of the mobility operator. When, $Re(\alpha_1) \ge 0$, the maximum growth rate is given by

$$\alpha_{\max} = -\frac{\|\mathbf{k}\|^2(3\gamma_1\|\mathbf{k}\|^2 + 2F_2(\phi_0, T_0))}{T_0^2(D_0 + C_A M F_2(\phi_0) + 2\gamma_1 C_A M\|\mathbf{k}\|^2)}(D_0 M T_0^2 - M_{13}^2 + M_{a,13}^2), \tag{3.12}$$

where $\|\mathbf{k}\|^2$ is given by the solution of equation

$$\begin{aligned} &\|\mathbf{k}\|^2\gamma_1 C_A M(D_0 - C_A M\beta) - \tfrac{2C_A(M_{13}^2 - M_{a,13}^2)}{T_0^2}(2F_2(\phi_0, T_0) + 3\gamma_1\|\mathbf{k}\|^2) \\ &+(D_0 + C_A M\beta + \gamma_1 C_A M\|\mathbf{k}\|^2)\sqrt{\Delta_\alpha} - (D_0 - C_A M\beta)^2 = 0. \end{aligned} \tag{3.13}$$

From the expression of α_1, we note that the magnitude of the potentially unstable growth rate depends on the mobility, in which $|M_{13}|$ tends to decrease $Re(\alpha_1)$ while $|M_{a,13}|$ tends to increase it while $Re(\alpha_1) > 0$. While $|M_{13}|$ is large enough to violate well-posedness constraint $M_{13}^2 > M D_0 T_0^2 + M_{a,13}^2$, $Re(\alpha_1) > 0$ in short wave range is proportional to $\|\mathbf{k}\|^2$, indicating the Hadamard instability.

In Fig. 3.1, we show the positive growth rates of the four models as functions of wave number $\|\mathbf{k}\|$, where the parameter values are chosen as follows

$$D_0 = 10^{-3},\ M = 10^{-3},\ C_A = 0.6,\ \gamma_1 = 10^{-3},\ \gamma_2 = 10^{-2},\ T_0 = 3. \tag{3.14}$$

Considering all four models, a consensus emerges: the role of cross-coupling mobility component M_{13} is to stabilize the steady state and enhance energy dissipation while the model is well-posed, i.e., it reduces the magnitude of the growth rate and decreases the energy dissipation rate; while cross-coupling parameter $M_{a,13}$ enhances instability of the steady state in the long-wave regime. This linear stability analysis also reveals that the model is ill-posed when $M_{13}^2 > M D_0 T_0^2 + M_{a,13}^2$, where the Hadamard instability ensues. This restriction on the parameter value of M_{13} must be heeded when applying the model.

We next discuss some structure-preserving numerical algorithms for model (2.20) that respects the entropy production rate regardless if it is positive or negative.

4. Numerical algorithms for thermodynamically consistent models

In this section, we derive discrete algorithms to approximate continuous PDEs given by (2.34) to achieve the goal of preserving entropy production rate. Firstly, we follow the idea of entropy quadratization method to introduce a new variable $q = \sqrt{-s_0 - \gamma_2\phi^2 - \gamma_3 e^2 + C_0}$, where C_0 is a positive constant large enough to make q well-defined [46]. In addition, the entropy of system (2.2) is expressed as a quadratic form

$$S = \int_\Omega (-\frac{\gamma_1}{2}|\nabla\phi|^2 - q^2 - \gamma_2\phi^2 - \gamma_3 e^2 + C_0) d\mathbf{x}. \tag{4.1}$$

Then we transform the general governing system of Eqs. (2.20) into an equivalent form,

$$\begin{cases} \phi_t + \nabla\cdot(\phi\mathbf{v}) = -\nabla\cdot[M\nabla(\gamma_1\Delta\phi - 2qq_\phi - 2\gamma_2\phi) + (M_{13}+M_{a,13})\nabla\frac{1}{T}], \\ \rho(\mathbf{v}_t + \mathbf{v}\cdot\nabla\mathbf{v}) = \nabla\cdot\sigma_e - \nabla p + \mathbf{F}_e, \\ \nabla\cdot\mathbf{v} = 0, \\ e_t + \mathbf{v}\cdot\nabla e = \sigma_e : \nabla\mathbf{v} - \nabla\cdot[(M_{13}-M_{a,13})\nabla(\gamma_1\Delta\phi - 2qq_\phi - 2\gamma_2\phi) + D_0T^2\nabla\frac{1}{T}], \\ q_t = q_\phi\phi_t + q_e e_t. \end{cases} \tag{4.2}$$

where $\sigma_e = -\gamma_1 T\nabla\phi\otimes\nabla\phi + 2\eta : T\mathbf{D}$, $e = C_A T$ and $q_\phi = \frac{\partial q}{\partial\phi}$, $q_e = \frac{\partial q}{\partial e}$.

4.1. Temporal discretization

We define the following the notations

$$\begin{aligned} &(\bullet)^{n+\frac{1}{2}} = \frac{1}{2}((\bullet)^{n+1} + (\bullet)^n), \quad \delta_t(\bullet)^{n+\frac{1}{2}} = \frac{1}{\Delta t}((\bullet)^{n+1} - (\bullet)^n), \\ &\overline{(\bullet)}^{n+\frac{1}{2}} = \frac{1}{2}(3(\bullet)^n - (\bullet)^{n-1}), \quad (\tilde{\bullet})^{n+\frac{1}{2}} = \frac{1}{2}((\tilde{\bullet})^{n+1} + (\bullet)^n). \end{aligned} \tag{4.3}$$

We apply the projection method to decouple the velocity field from the pressure field and the Crank–Nicolson method to discretize the time derivative of the equations to yield a second order entropy-production-rate-preserving scheme.

Scheme 1 (*Semi-Implicit Pressure Projection-Type and Entropy-Production-Rate-Preserving Scheme*). *Given $\mathbf{v}^n$, ϕ^n, T^n and p^n, we update $\mathbf{v}^{n+1}$, ϕ^{n+1}, T^{n+1} and p^{n+1} as below:*

$$\begin{aligned} &Step\ 1 : Update\ \mathbf{v}^{n+1}, p^{n+1}\ via \\ &\begin{cases} \frac{\rho}{\Delta t}(\tilde{\mathbf{v}}^{n+1} - \mathbf{v}^n) + \rho\bar{\mathbf{v}}^{n+\frac{1}{2}}\cdot\nabla\tilde{\mathbf{v}}^{n+\frac{1}{2}} = \nabla\cdot\overline{\sigma_e}^{n+\frac{1}{2}} - \nabla p^n + \overline{\mathbf{F}_e}^{n+\frac{1}{2}}, \\ \\ \frac{\rho}{\Delta t}(\mathbf{v}^{n+1} - \tilde{\mathbf{v}}^{n+1}) = -\frac{1}{2}\nabla(p^{n+1} - p^n), \quad \nabla\cdot\mathbf{v}^{n+1} = 0, \end{cases} \\ &where\ \tilde{\mathbf{v}}^{n+1}|_{\partial\Omega} = 0; \\ &Step\ 2 :: Update\ \phi^{n+1}, e^{n+1}\ and\ q^{n+1}\ by \\ &\begin{cases} \delta_t\phi^{n+\frac{1}{2}} + \nabla\cdot(\phi^{n+\frac{1}{2}}\mathbf{v}^{n+\frac{1}{2}}) = -\nabla\cdot[M\nabla\frac{\delta S}{\delta\phi}^{n+\frac{1}{2}} + (M_{13}+M_{a,13})\nabla(\frac{1}{T})^{n+\frac{1}{2}}], \\ \delta_t e^{n+\frac{1}{2}} + \mathbf{v}^{n+\frac{1}{2}}\cdot\nabla e^{n+\frac{1}{2}} = \sigma_e^{n+\frac{1}{2}} : \nabla\mathbf{v}^{n+\frac{1}{2}} - \nabla\cdot[(M_{13}-M_{a,13})\nabla\frac{\delta S}{\delta\phi}^{n+\frac{1}{2}} + D_0(T^{n+\frac{1}{2}})^2\nabla(\frac{1}{T})^{n+\frac{1}{2}}], \\ \delta_t q^{n+\frac{1}{2}} = \bar{q}_\phi^{n+\frac{1}{2}}\delta_t\phi^{n+\frac{1}{2}} + \bar{q}_e^{n+\frac{1}{2}}\delta_t e^{n+\frac{1}{2}}, \end{cases} \end{aligned} \tag{4.4}$$

where

$$\begin{aligned} &\sigma_e^{n+\frac{1}{2}} = -\gamma_1 T^{n+\frac{1}{2}}\nabla\phi^{n+\frac{1}{2}}\otimes\nabla\phi^{n+\frac{1}{2}} + 2\eta^{n+\frac{1}{2}} : T^{n+\frac{1}{2}}\mathbf{D}^{n+\frac{1}{2}}, \\ &\frac{\delta S}{\delta\phi}^{n+\frac{1}{2}} = \gamma_1\Delta\phi^{n+\frac{1}{2}} - 2q^{n+\frac{1}{2}}\bar{q}_\phi^{n+\frac{1}{2}} - 2\gamma_2\phi^{n+\frac{1}{2}}, e^{n+\frac{1}{2}} = C_A T^{n+\frac{1}{2}}. \end{aligned} \tag{4.5}$$

The following theorem shows that the scheme is entropy-production-rate-preserving.

Theorem 4.1. *Semi-implicit pressure projection-type and entropy-production-rate-preserving scheme preserves the entropy production rate*

$$\begin{aligned} &\frac{S^{n+1}-S^n}{\Delta t} = \int_\Omega[M(\nabla\frac{\delta S}{\delta\phi}^{n+\frac{1}{2}})^2 + 2\eta^{n+\frac{1}{2}} : T^{n+\frac{1}{2}}\mathbf{D}^{n+\frac{1}{2}} : \mathbf{D}^{n+\frac{1}{2}} + D_0(T^{n+\frac{1}{2}})^2(\nabla(\frac{1}{T})^{n+\frac{1}{2}})^2 \\ &+2M_{13}\nabla\frac{\delta S}{\delta\phi}^{n+\frac{1}{2}}\nabla\frac{1}{T}^{n+\frac{1}{2}}]d\mathbf{x} + \int_{\partial\Omega}\mathbf{n}\cdot[(-\gamma_1\nabla\phi^{n+\frac{1}{2}})\delta_t\phi^{n+\frac{1}{2}} - \mathbf{q}^{n+\frac{1}{2}}(\frac{1}{T})^{n+\frac{1}{2}} - \frac{\delta S}{\delta\phi}^{n+\frac{1}{2}}J^{n+\frac{1}{2}} \\ &-(s^{n+\frac{1}{2}}\mathbf{I} - \frac{\partial s}{\partial\nabla\phi}^{n+\frac{1}{2}}\nabla\phi^{n+\frac{1}{2}})\cdot\mathbf{v}^{n+\frac{1}{2}}]d\mathbf{a}, \end{aligned} \tag{4.6}$$

where

$$\begin{aligned} &J^n = M\nabla\frac{\delta S}{\delta\phi}^n + (M_{13}+M_{a,13})\nabla(\frac{1}{T})^n, \\ &\mathbf{q}^n = (M_{13}-M_{a,13})\nabla\frac{\delta S}{\delta\phi}^n + D_0(T^n)^2\nabla(\frac{1}{T})^n, \\ &S^n = \int_\Omega[-|q^n|^2 - \gamma_2|\phi^n|^2 - \gamma_3|e^n|^2 - \frac{\gamma_1}{2}|\nabla\phi^n|^2 + C_0]d\mathbf{x}. \end{aligned} \tag{4.7}$$

Proof. Using (4.7) and the Green's formula, we arrive at the following result

$$\begin{aligned}&\frac{S^{n+1}-S^n}{\Delta t}\\&=\int_\Omega[-2q^{n+\frac{1}{2}}\frac{q^{n+1}-q^n}{\Delta t}-2\gamma_2\phi^{n+\frac{1}{2}}\frac{\phi^{n+1}-\phi^n}{\Delta t}-2\gamma_3 e^{n+\frac{1}{2}}\frac{e^{n+1}-e^n}{\Delta t}-\gamma_1\nabla\phi^{n+\frac{1}{2}}\frac{\nabla\phi^{n+1}-\nabla\phi^n}{\Delta t}]d\mathbf{x}\\&=\int_\Omega(\delta_t\phi^{n+\frac{1}{2}}\frac{\delta S}{\delta\phi}^{n+\frac{1}{2}}+\delta_t e^{n+\frac{1}{2}}\frac{\delta S}{\delta e}^{n+\frac{1}{2}})d\mathbf{x}-\int_{\partial\Omega}\gamma_1\mathbf{n}\cdot\nabla\phi^{n+\frac{1}{2}}\delta_t\phi^{n+\frac{1}{2}}d\mathbf{a}.\end{aligned}\tag{4.8}$$

Next, taking inner product of the first equation in $Step$ 2 with $\frac{\delta S}{\delta\phi}^{n+\frac{1}{2}}$, we obtain

$$\begin{aligned}&\int_\Omega\delta_t\phi^{n+\frac{1}{2}}\frac{\delta S}{\delta\phi}^{n+\frac{1}{2}}d\mathbf{x}=\int_\Omega[M(\nabla\frac{\delta S}{\delta\phi}^{n+\frac{1}{2}})^2+(M_{13}+M_{a,13})\nabla(\frac{1}{T})^{n+\frac{1}{2}}\nabla\frac{\delta S}{\delta\phi}^{n+\frac{1}{2}}]d\mathbf{x}\\&-\int_\Omega\nabla\cdot(\phi^{n+\frac{1}{2}}\mathbf{v}^{n+\frac{1}{2}})\frac{\delta S}{\delta\phi}^{n+\frac{1}{2}}d\mathbf{x}-\int_{\partial\Omega}\mathbf{n}\cdot[M\nabla\frac{\delta S}{\delta\phi}^{n+\frac{1}{2}}+(M_{13}+M_{a,13})\nabla(\frac{1}{T})^{n+\frac{1}{2}}]\frac{\delta S}{\delta\phi}^{n+\frac{1}{2}}d\mathbf{a}.\end{aligned}\tag{4.9}$$

Taking inner product of the second equation in $Step$ 2 with $\frac{\delta S}{\delta e}^{n+\frac{1}{2}}$, we have

$$\begin{aligned}&\int_\Omega\delta_t e^{n+\frac{1}{2}}\frac{\delta S}{\delta e}^{n+\frac{1}{2}}d\mathbf{x}\\&=\int_\Omega[(M_{13}-M_{a,13})\nabla\frac{\delta S}{\delta\phi}^{n+\frac{1}{2}}\nabla(\frac{1}{T})^{n+\frac{1}{2}}+D_0(T^{n+\frac{1}{2}})^2(\nabla(\frac{1}{T})^{n+\frac{1}{2}})^2]d\mathbf{x}\\&-\int_\Omega(\mathbf{v}^{n+\frac{1}{2}}\cdot\nabla e^{n+\frac{1}{2}})\frac{\delta S}{\delta e}^{n+\frac{1}{2}}d\mathbf{x}+\int_\Omega\frac{\delta S}{\delta e}^{n+\frac{1}{2}}\sigma_e^{n+\frac{1}{2}}:\nabla\mathbf{v}^{n+\frac{1}{2}}d\mathbf{x}\\&-\int_{\partial\Omega}\mathbf{n}\cdot[(M_{13}-M_{a,13})\nabla\frac{\delta S}{\delta\phi}^{n+\frac{1}{2}}+D_0(T^{n+\frac{1}{2}})^2\nabla(\frac{1}{T})^{n+\frac{1}{2}}]\frac{\delta S}{\delta e}^{n+\frac{1}{2}}d\mathbf{a}.\end{aligned}\tag{4.10}$$

Noticing $\nabla\cdot\mathbf{v}^{n+\frac{1}{2}}=0$, we give the discrete form of Eq. (2.9) as follows

$$\begin{aligned}&(\frac{\delta S}{\delta e}^{n+\frac{1}{2}}\nabla e^{n+\frac{1}{2}}+\frac{\delta S}{\delta\phi}^{n+\frac{1}{2}}\nabla\phi^{n+\frac{1}{2}})\cdot\mathbf{v}^{n+\frac{1}{2}}\\&=\frac{\partial s}{\partial\nabla\phi}^{n+\frac{1}{2}}\nabla\phi^{n+\frac{1}{2}}:\nabla\mathbf{v}^{n+\frac{1}{2}}+\nabla\cdot[(s^{n+\frac{1}{2}}\mathbf{I}-\frac{\partial s}{\partial\nabla\phi}^{n+\frac{1}{2}}\nabla\phi^{n+\frac{1}{2}})\cdot\mathbf{v}^{n+\frac{1}{2}}].\end{aligned}\tag{4.11}$$

Based on the above result (4.11), we deduce

$$\begin{aligned}&\int_\Omega[\nabla\cdot(\phi^{n+\frac{1}{2}}\mathbf{v}^{n+\frac{1}{2}})\frac{\delta S}{\delta\phi}^{n+\frac{1}{2}}+(\mathbf{v}^{n+\frac{1}{2}}\cdot\nabla e^{n+\frac{1}{2}})\frac{\delta S}{\delta e}^{n+\frac{1}{2}}]d\mathbf{x}\\&=\int_\Omega[\frac{\partial s}{\partial\nabla\phi}^{n+\frac{1}{2}}\nabla\phi^{n+\frac{1}{2}}:\nabla\mathbf{v}^{n+\frac{1}{2}}]d\mathbf{x}+\int_{\partial\Omega}\mathbf{n}\cdot(s^{n+\frac{1}{2}}\mathbf{I}-\frac{\partial s}{\partial\nabla\phi}^{n+\frac{1}{2}}\nabla\phi^{n+\frac{1}{2}})\cdot\mathbf{v}^{n+\frac{1}{2}}d\mathbf{a}.\end{aligned}\tag{4.12}$$

Finally, substituting(4.9) (4.10) into (4.8) and combining with (4.12), we arrive at

$$\begin{aligned}&\frac{S^{n+1}-S^n}{\Delta t}=\int_\Omega[M(\nabla\frac{\delta S}{\delta\phi}^{n+\frac{1}{2}})^2+2\eta^{n+\frac{1}{2}}:T^{n+\frac{1}{2}}\mathbf{D}^{n+\frac{1}{2}}:\mathbf{D}^{n+\frac{1}{2}}+D_0(T^{n+\frac{1}{2}})^2(\nabla(\frac{1}{T})^{n+\frac{1}{2}})^2\\&+2M_{13}\nabla\frac{\delta S}{\delta\phi}^{n+\frac{1}{2}}\nabla\frac{1}{T}^{n+\frac{1}{2}}]d\mathbf{x}-\int_{\partial\Omega}\mathbf{n}\cdot[M\nabla\frac{\delta S}{\delta\phi}^{n+\frac{1}{2}}+(M_{13}+M_{a,13})\nabla(\frac{1}{T})^{n+\frac{1}{2}}]\frac{\delta S}{\delta\phi}^{n+\frac{1}{2}}d\mathbf{a}\\&+\int_{\partial\Omega}\mathbf{n}\cdot(-\gamma_1\nabla\phi^{n+\frac{1}{2}})\delta_t\phi^{n+\frac{1}{2}}d\mathbf{a}-\int_{\partial\Omega}\mathbf{n}\cdot(s^{n+\frac{1}{2}}\mathbf{I}-\frac{\partial s}{\partial\nabla\phi}^{n+\frac{1}{2}}\nabla\phi^{n+\frac{1}{2}})\cdot\mathbf{v}^{n+\frac{1}{2}}d\mathbf{a}\\&-\int_{\partial\Omega}\mathbf{n}\cdot[(M_{13}-M_{a,13})\nabla\frac{\delta S}{\delta\phi}^{n+\frac{1}{2}}+D_0(T^{n+\frac{1}{2}})^2\nabla(\frac{1}{T})^{n+\frac{1}{2}}](\frac{1}{T})^{n+\frac{1}{2}}d\mathbf{a}.\end{aligned}\tag{4.13}$$

Hence, this completes the proof.

Remark 4.1. With the discrete adiabatic boundary conditions:

$$\mathbf{n}\cdot\nabla\phi^n\mid_{\partial\Omega}=0,\quad\mathbf{v}^n\mid_{\partial\Omega}=0,\quad\mathbf{n}\cdot\nabla\frac{\delta S}{\delta\phi}^n\mid_{\partial\Omega}=0,\quad\mathbf{n}\cdot\nabla T^n\mid_{\partial\Omega}=0\ (n=0,1,\ldots,N),\tag{4.14}$$

and the mobility operator $\mathcal{M}\geq 0$, the entropy production rate of system can be written into

$$\begin{aligned}\frac{S^{n+1}-S^n}{\Delta t}&=\int_\Omega[M(\nabla\frac{\delta S}{\delta\phi}^{n+\frac{1}{2}})^2++2\eta^{n+\frac{1}{2}}:T^{n+\frac{1}{2}}\mathbf{D}^{n+\frac{1}{2}}:\mathbf{D}^{n+\frac{1}{2}}+D_0(T^{n+\frac{1}{2}})^2(\nabla(\frac{1}{T})^{n+\frac{1}{2}})^2\\&+2M_{13}\nabla\frac{\delta S}{\delta\phi}^{n+\frac{1}{2}}\nabla\frac{1}{T}^{n+\frac{1}{2}}]d\mathbf{x}\geq 0,\end{aligned}\tag{4.15}$$

and the volume change rate of fluid 1

$$\frac{V^{n+1}-V^n}{\Delta t}=\int_\Omega\frac{\phi^{n+1}-\phi^n}{\Delta t}d\mathbf{x}=0.\tag{4.16}$$

So, it indicates that the scheme yields a positive entropy production rate and volume conservation under the adiabatic BCs at the semi-discrete level.

Furthermore, using finite difference methods on staggered grids, we discretize the above semi-discrete scheme spatially to arrive at the corresponding fully discrete scheme. We also demonstrate that the fully discrete scheme preserves the properties of the entropy-production-rate under suitable boundary conditions. We adopt the notations defined in [39] and omit the detail to save space.

4.2. Spatial discretization

Applying the staggered-grid finite difference discretization in space to semi-discrete Scheme 1, we obtain the following fully discrete scheme:

Scheme 2 (*Fully Discrete Pressure Projection-Type and Entropy-Production-Rate-Preserving Scheme*).*Given* $\mathbf{v}_h^n$, ϕ_h^n, T_h^n *and* p_h^n, *we update* $\mathbf{v}_h^{n+1}$, ϕ_h^{n+1}, T_h^{n+1} *and* p_h^{n+1} *as below:*

$$
\begin{array}{l}
Step\ 1 : Update\ \mathbf{v}_h^{n+1}, p_h^{n+1}\ via\\
\begin{cases}
\frac{\rho}{\Delta t}(\tilde{\mathbf{v}}_h^{n+1}-\mathbf{v}_h^n)+\rho\bar{\mathbf{v}}_h^{n+\frac{1}{2}}\cdot\nabla_h\tilde{\mathbf{v}}_h^{n+\frac{1}{2}}=\nabla_h\cdot\sigma_e^{n+\frac{1}{2}}-\nabla_h p_h^n+\mathbf{F}_e^{n+\frac{1}{2}},\\
\frac{\rho}{\Delta t}(\mathbf{v}_h^{n+1}-\tilde{\mathbf{v}}_h^{n+1})=-\frac{1}{2}\nabla_h(p_h^{n+1}-p_h^n),\quad \nabla_h\cdot\mathbf{v}_h^{n+1}=0,
\end{cases}\\
where\ \tilde{\mathbf{v}}_h^{n+1}\mid_{\partial\Omega}=0;\\
Step\ 2 :: Update\ \phi_h^{n+1}, e_h^{n+1}\ and\ q_h^{n+1}\ by\\
\begin{cases}
\delta_t\phi_h^{n+\frac{1}{2}}+\nabla_h\cdot(\phi_h^{n+\frac{1}{2}}\mathbf{v}_h^{n+\frac{1}{2}})=-\nabla_h\cdot[M\nabla_h\frac{\delta S}{\delta\phi}^{n+\frac{1}{2}}+(M_{13}+M_{a,13})\nabla_h(\frac{1}{T})^{n+\frac{1}{2}}],\\
\delta_t e_h^{n+\frac{1}{2}}+\mathbf{v}_h^{n+\frac{1}{2}}\cdot\nabla_h e_h^{n+\frac{1}{2}}=\sigma_e^{n+\frac{1}{2}}:\nabla_h\mathbf{v}_h^{n+\frac{1}{2}}-\nabla_h\cdot[(M_{13}-M_{a,13})\nabla_h\frac{\delta S}{\delta\phi}^{n+\frac{1}{2}}\\
\qquad\qquad +D_0(T^{n+\frac{1}{2}})^2\nabla_h(\frac{1}{T})^{n+\frac{1}{2}}],\\
q_h^{n+1}-q_h^n=\bar{q}_\phi^{n+\frac{1}{2}}(\phi_h^{n+1}-\phi_h^n)+\bar{q}_e^{n+\frac{1}{2}}(e_h^{n+1}-e_h^n),
\end{cases}
\end{array}
\tag{4.17}
$$

where

$$
\begin{array}{l}
\sigma_e^{n+\frac{1}{2}}=-\gamma_1 T_h^{n+\frac{1}{2}}\nabla_h\phi_h^{n+\frac{1}{2}}\otimes\nabla_h\phi_h^{n+\frac{1}{2}}+2\eta^{n+\frac{1}{2}}:T_h^{n+\frac{1}{2}}\mathbf{D}_h^{n+\frac{1}{2}},\\
\frac{\delta S}{\delta\phi}^{n+\frac{1}{2}}=\gamma_1\Delta_h\phi_h^{n+\frac{1}{2}}-2q_h^{n+\frac{1}{2}}\bar{q}_\phi^{n+\frac{1}{2}}-2\gamma_2\phi_h^{n+\frac{1}{2}}, e_h^{n+\frac{1}{2}}=C_A T_h^{n+\frac{1}{2}}.
\end{array}
\tag{4.18}
$$

Theorem 4.2. *The fully discrete scheme preserves the entropy production rate. Specially, given fully discrete boundary conditions* (4.14)*:*

$$
u^n,\ D_x\phi^n,\ D_x\frac{\delta S}{\delta\phi}^n,\ D_xT^n\in\varepsilon_{x\times y}^{ew0},\quad v^n,\ D_y\phi^n,\ D_y\frac{\delta S}{\delta\phi}^n,\ D_yT^n\in\varepsilon_{x\times y}^{ns0}
\tag{4.19}
$$

and the mobility operator $\mathcal{M}\geq 0$, *the fully discrete scheme preserves the volume conservation law:* $V_h^{n+1}=V_h^n$, *and yields a positive entropy production rate*

$$
\begin{array}{l}
\frac{S_h^{n+1}-S_h^n}{\Delta t}=(M\nabla_h\frac{\delta S}{\delta\phi}^{n+\frac{1}{2}},\nabla_h\frac{\delta S}{\delta\phi}^{n+\frac{1}{2}})_2+(D_0(T^{n+\frac{1}{2}})^2\nabla_h(\frac{1}{T})^{n+\frac{1}{2}},\nabla_h(\frac{1}{T})^{n+\frac{1}{2}})_2\\
+(2\eta^{n+\frac{1}{2}}T^{n+\frac{1}{2}},[(d_xu^{n+\frac{1}{2}})^2+\frac{1}{2}(a_xD_xa_yv^{n+\frac{1}{2}}+a_yD_ya_xu^{n+\frac{1}{2}})^2+(d_yv^{n+\frac{1}{2}})^2])_2\\
+(2M_{13}\nabla\frac{\delta S}{\delta\phi}^{n+\frac{1}{2}},\nabla_h\frac{1}{T}^{n+\frac{1}{2}})\geq 0,
\end{array}
\tag{4.20}
$$

where

$$
V_h^n=(\phi^n,1)_2,\quad S_h^n=-\|q^n\|_2^2-\gamma_2\|\phi^n\|_2^2-\gamma_3\|e^n\|_2^2-\frac{\gamma_1}{2}\|\nabla_h\phi^n\|_2^2+(C_0,1)_2.
\tag{4.21}
$$

Proof. The proof is similar to the proof of Theorem 3.3 in our previous work [27]. Thus, we omit the detail to save space in this paper.

Remark 4.2. It implies that the scheme yields a positive entropy production rate and volume conservation under adiabatic BCs at the fully discrete level.

5. Numerical results and discussion

In this section, we implement the numerical schemes for models under two different boundary conditions to verify the thermodynamical consistency, accuracy of the scheme, volume conservation, and entropy product rate preserving property of the schemes numerically. We then use them to study the cross-coupling effect between the phase field and the temperature field in the nonlinear regime. In all numerical experiments, we fix computational domain $\Omega=[0,2\pi]^2$ and the initial states as follows

$$
\begin{array}{l}
\mathbf{v}(x,y,0)=(0,0),\ T(x,y,0)=3,\\
\phi(x,y,0)=\tanh(\frac{y-y_1(x)}{0.2})\tanh(\frac{y-y_2(x)}{0.2}),\\
y_1=\pi-(1+0.1cos(x)), y_2=\pi+(1+0.1cos(x)).
\end{array}
\tag{5.1}
$$

Unless otherwise specified, we set model parameter values as $\gamma_1=10^{-3}$, $\gamma_3=1$, $C_0=10^4,\rho=1,C_A=0.6,\eta_0^{(1)}=0.05,\eta_0^{(2)}=0.1,E_a^{(1)}=1,E_a^{(2)}=0.5,R=1$ and the cross-coupling parameters for each model in Model 1: $M_{13}=0$, $M_{a,13}=0$, in Model 2: $M_{13}=10^{-3}$, $M_{a,13}=0$, in Model 3: $M_{13}=0$, $M_{a,13}=10^{-3}$, and in Model 4: $M_{13}=10^{-3}$, $M_{a,13}=2.5\times10^{-3}$, wherever relevant.

5.1. Temporal mesh refinement test

To confirm the order of convergence of the scheme, we conduct several time-step refinement tests. Without loss of generality, we show the accuracy of the numerical scheme constructed based on Model 2 and $\gamma_2=1, D_0=10^{-5}$. We choose the number of spatial meshes as $N_x=N_y=128$, time steps $\Delta t=10^{-3}\times\frac{1}{2^{k-1}}, k=1,\ldots,7$, respectively. At final time $t=0.01$, we calculate differences of ϕ, T and u, v between consecutive time steps in the L^2 norm, respectively. The numerical results of the mesh refinement test are summarized in Fig. 5.1, from which the second-order convergence rate for all variables in time are observed. The spatial mesh refinement test shows a similar result with slope 2 and is omitted to save space.

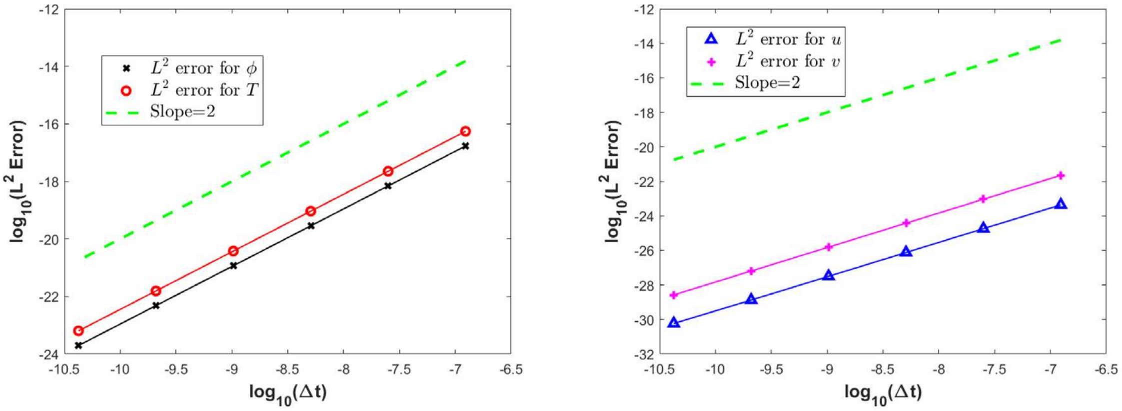

(a) Convergence test for ϕ and T.

(b) Convergence test for u and v.

Fig. 5.1. Temporal convergence test of the scheme. (a): The error of ϕ and T. (b): The error of u and v. The second-order convergence rate in time for all variables are confirmed.

5.2. Cross-coupling between phase and temperature under adiabatic boundary conditions

We investigate the effect of cross-coupling between the phase field and temperature field in the nonlinear regime of the system by contrasting solutions of the models with adiabatic boundary conditions. We begin with the case without an external force and then study the one with a buoyant force obtained from the Boussinesq approximation given by $\mathbf{F}_e = \rho \kappa T g \mathbf{z}$, where g is the gravitational acceleration, $\mathbf{z}$ is the unit vector in the direction of gravity and κ is a small thermal expansion coefficient.

We set parameter values as follows: $\gamma_2 = 10^{-2}, D_0 = 10^{-3}, \kappa = 3.4 \times 10^{-2}, g = 9.8$ and the number of spatial meshes as $N_x = N_y = 128$. In the numerical simulations, we implement an adaptive time-stepping strategy and set the maximum and minimum adaptive time steps as $\Delta t_{max} = 1$ and $\Delta t_{min} = 1.0 \times 10^{-3}$, respectively.

Firstly, Fig. 5.2 displays snapshots of the velocity and phase fields obtained from Model 1 without the external force. The other three models yield similar results such that their results are omitted. In all cases, four roll cells are present near the two interfaces, and the interface shapes are nearly identical across all four models. While the phase and velocity fields are qualitatively similar among the models, the temperature field exhibit notable differences. Fig. 5.3 illustrates the temperature distributions at four selected time points of each model:

- Model 1: Due to the roll cells, lower and higher temperature regions alternate around the two interfaces, where the heat conduction coefficient is D_0.
- Model 2: The effective heat conduction coefficient is $\frac{M_{13} C_A}{T^2} + D_0$. A positive M_{13} enhances heat conductivity, while a negative one reduces it. The results show that enhanced heat conduction creates two low-temperature layers near the interfaces, encapsulating the phase 1 fluid region and leading to increased temperature within it.
- Model 3: The effective heat conduction coefficient is $-\frac{M_{a,13} C_A}{T^2} + D_0$. A positive $M_{a,13}$ reduces heat conductivity, creating higher temperature layers at the interfaces. These layers extract heat from the phase 1 fluid region. When the signs of M_{13} and $M_{a,13}$ reverse, the observed effects also reverse.
- Model 4: The behavior of Model 4 is similar to Model 3 qualitatively, given that the parameter value of $M_{a,13}$ is larger than M_{13} and both are positive.

When gravity is absent in the model, the solutions exhibit symmetries in the vertical direction. We next investigate how buoyant force due to gravity breaks the symmetry, inducing nonlinear, spatial instability.

Fig. 5.4 shows snapshots of the velocity and phase field obtained from Model 1, 2, 3 with buoyant force $\mathbf{F}_e$. By comparing Fig. 5.2 with Fig. 5.4, we observe that the buoyant force due to temperature variations has a noticeable effect on interface dynamics. Initially, the simulations reveal the formation of four roll cells near the interfaces in the velocity field, where fluid convection is primarily induced by the buoyant force. When cross-coupling is absent, the temperature variation in the time interval investigated is small, in which the interface dynamics are not altered noticeably. However, when cross-coupling is present, the temperature variation enhances in the computational domain so that it affects the buoyant force spatially, which in turn alters the interface location significantly.

For Model 2, flows in the top part are enhanced more than in the bottom part due to enhanced dissipation by a nonzero M_{13} so that the dynamics in the active region deform the interface more significantly. The higher temperature region occupied by phase 1 fluids tends to mix more with the cooler region above it than with the cooler region below it due to Rayleigh–Bénard convection. So the top interface is deformed much more than the bottom one.

For Model 3, the scenario is reversed qualitatively under the influence of enhanced convection. The cooler fluid in the region of phase 1 tends to sediment to the region of hotter fluid so that the bottom interface is deformed more than the top one. This is a manifestation of Rayleigh–Bénard convection in the computational domain.

To further demonstrate the transport mechanism described by the model, we examine two fluxes: the material flux of the model, $\psi_{flux} = M \nabla \frac{\delta S}{\delta \phi} + (M_{13} + M_{a,13}) \nabla \frac{1}{T} + \phi \mathbf{v}$; and the energy flux of the model, $\omega_{flux} = (M_{13} - M_{a,13}) \nabla \frac{\delta S}{\delta \phi} + D_0 T^2 \nabla \frac{1}{T} + e\mathbf{v}$. Fig. 5.6 depicts the energy flux highlighting how energy is distributed in the flow field dynamically.

For Model 1, the four roll cells survive up to the time we stop the computation which leads to five low energy spots and 6 high energy spots along the path of energy flows. Cross-coupling destroys the structure creating a pair of roll cells circling around two low energy spots which sandwich a

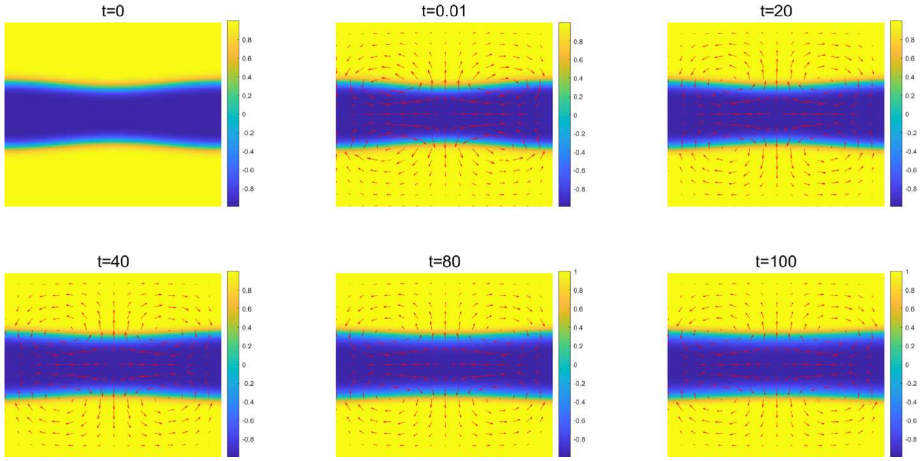

Fig. 5.2. Snapshots of the velocity and phase field obtained from Model 1 without the external force. Four roll cells are present in the vicinity of both interfaces over time. The shape of the interfaces does not change much for all other models (Model 2, 3, 4).

single high energy spot. Material fluxes depicted in Fig. 5.7 support the energy redistribution dynamics in the later stage of the simulation. At the places of high energy activities, materials are more concentrated.

Fig. 5.5 shows the velocity and temperature distribution of Model 2 and 3. The cross-coupling in Model 2 tends to excite the top part more than the bottom one, making the phase in the middle hotter than the other phase. It then fuses the active dynamics in the upper interface between the two phases. The entropy conservative cross-coupling in Model 3 exhibits exactly the opposite effect to the temperature and the flow field.

Next, when $M_{a,13}$ in Model 3 increases from 10^{-3} to 10^{-2}, the phase field and temperature field are shown in Fig. 5.8 Row 3 and Row 4, respectively. By comparing the dynamic processes of Model 3 (Fig. 5.8 Row 3) and Model 4 (Fig. 5.8 Row 1), the interface dynamics of Model 3 ($M_{a,13} = 10^{-2}$) at$t = 60$ is the same as that of Model 4 at t=240, which also coincides with the theoretical results on the growth rate ((Fig. 3.1(b)). The result shows that the dynamic process of Model 3 increases significantly, in fact much higher than that of Model 4. These numerical simulations agree with our theoretical results of the linear stability analysis in Fig. 3.1.

Subsequently, we show that the numerical schemes preserve both volume and positive entropy production rate for the four models in Fig. 5.9, consistent with the theoretical results. Furthermore, Fig. 5.10 presents the time step distribution in our adaptive step strategy throughout the simulation of the solution for $0 \leq t \leq 300$ to benchmark the performance of the scheme.

5.3. Cross-coupling between phase and temperature with nonadiabatic boundary conditions

In the second numerical experiment, we investigate the effect of cross-coupling by contrasting the solutions of Model 1, 2 and 3 in the nonisothermal binary fluid system under a non-adiabatic boundary condition, where different temperature values are prescribed at the top and bottom boundary while no-flux boundary conditions are given at other parts of the boundary, respectively.

Fig. 5.11 shows snapshots of the velocity and phase field of Model 1 with $M_{13} = 0, M_{a,13} = 0$, Model 2 with $M_{13} = 10^{-3}, M_{a,13} = 0$ and Model 3 with $M_{13} = 0, M_{a,13} = 10^{-3}$, respectively. For all three models, throughout the simulations, fluid convection prevails influenced by the buoyant force. Moreover, we observe that cross-coupling has a visible effect on the interface dynamics. When cross-coupling is absent (Model 1), the fluid at the bottom is heated up, its density decreases, so the buoyant force pushes the less-dense fluid up towards the cooler end of the domain. Meanwhile, the cooler fluid at the top is denser, so it sediments due to gravity to displace the warmer fluid underneath.

However, when cross-coupling is present (e.g., Model 2 and Model 3), the temperature field in the domain is significantly different from Model 1 after a while so that it affects the buoyant force spatially which in turn alters the mixing of the fluids. The comparison with the numerical results of Model 1 shows that fluid mixing is enhanced in Model 2. However, the comparison with the numerical results of Model 1 shows that the mixing effect is slightly weakened in Model 3.

Fig. 5.12 shows the velocity and temperature distribution of the three models. The entropy production enhancing cross-coupling (Model 2) tends to have more dramatic temperature changes than Model 1. The entropy conservative cross-coupling (Model 3) exhibits less dramatic changes in the temperature field than Model 1.

6. Conclusion

In this paper, we have established a comprehensive framework for modeling nonisothermal binary viscous fluids encompassing model derivation and thermodynamically consistent numerical approximations, guided by the generalized Onsager principle and conservation laws. The incorporation of cross-coupling effects between phase, temperature, and velocity in the model allows a more realistic representation of fluid behaviors under varying real-world conditions. We have analyzed a special limit with the phase and temperature coupling and proposed necessary thermodynamical conditions for well-posedness of the model. Based on the entropy variational formulation of the model and entropy quadratization strategy, we introduce a structure-preserving numerical algorithm for numerically solving the model. Numerical simulations are conducted on the limiting model with phase-temperature coupling. Our numerical simulations reveal the intriguing symmetry-breaking phenomena and stabilizing and destabilizing effects due to the combination of cross-coupling and Rayleigh–Bénand convection, and in the meantime showcase two potential physical processes of the phase-temperature coupling: entropy-enhancing and entropy preserving coupling. The model and numerical algorithms constitute a versatile framework applicable to a myriad of real-world scenarios involving multiphasic fluid flows where non-isothermal effects play a pivotal role. In materials science, manipulating these couplings could lead to tailored properties in composite materials, while in geophysics, understanding these

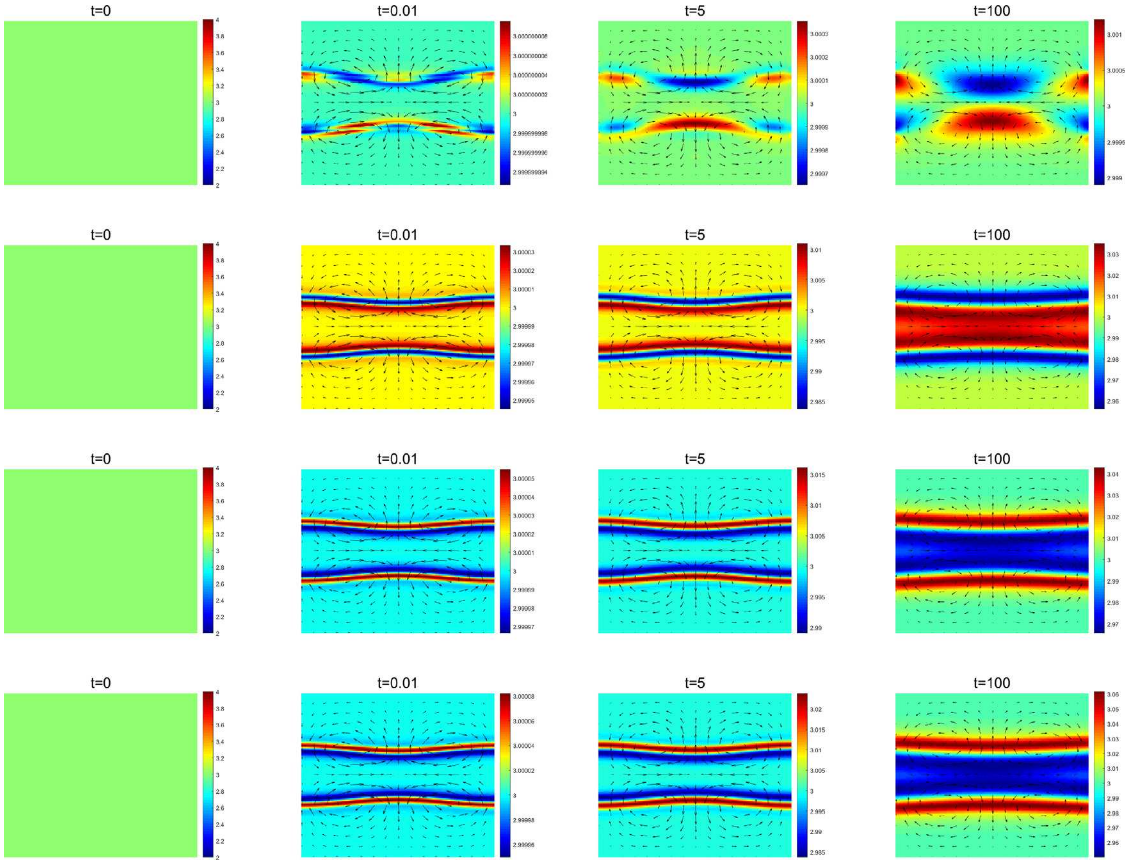

Fig. 5.3. Snapshots of the temperature and velocity field of Model 1–4 without the external force at $t = 0, 0.01, 5, 100$, respectively. Row 1: Model 1 with $M_{13} = 0, M_{a,13} = 0$. Row 2: Model 2 with $M_{13} = 10^{-3}, M_{a,13} = 0$. Row 3: Model 3 with $M_{13} = 0, M_{a,13} = 10^{-3}$. Row 4: Model 4 with $M_{13} = 10^{-3}$, $M_{a,13} = 2.5 \times 10^{-3}$. All solutions are symmetric in the vertical direction. Model 1 has an inter-digitated pattern of low and high temperature regions around the interfaces. Model 2 has a higher temperature region in phase 1 sandwiched by two layers of lower temperature regions at the interfaces. Model 3 has a lower temperature region in phase 1 sandwiched by two layers of higher temperature regions at the interfaces. The temperature distribution pattern in Model 4 is qualitatively the same as that of Model 3.

interactions may enhance predictions of natural phenomena like magma flow and sediment transport. Overall, the combination of our robust theoretical framework and the efficient numerical algorithms establishes a versatile tool for researchers and engineers dealing with multiphasic fluid flows influenced by nonisothermal coupling effects.

CRediT authorship contribution statement

Shouwen Sun: Writing – original draft, Validation, Software. **Jun Li:** Methodology. **Qi Wang:** Writing – review & editing, Supervision, Methodology, Conceptualization.

Declaration of competing interest

The authors declare that they have no known competing financial interests or personal relationships that could have appeared to influence the work reported in this paper.

Acknowledgments

Shouwen Sun's work is supported by the International Scientific and Technological Cooperation Projects of Henan Province 252102520010, National Natural Science Foundation of China 12101387 and Henan International Joint Laboratory of Optical Information Transmission and Application. Jun Li's work is supported by The Science & Technology Development Fund of Tianjin Education Commission for Higher Education 2020KJ005. Qi Wang's research is partially supported by the National Science Foundation of US awards DMS-2038080 and OIA-2242812.

Data availability

Data will be made available on request.

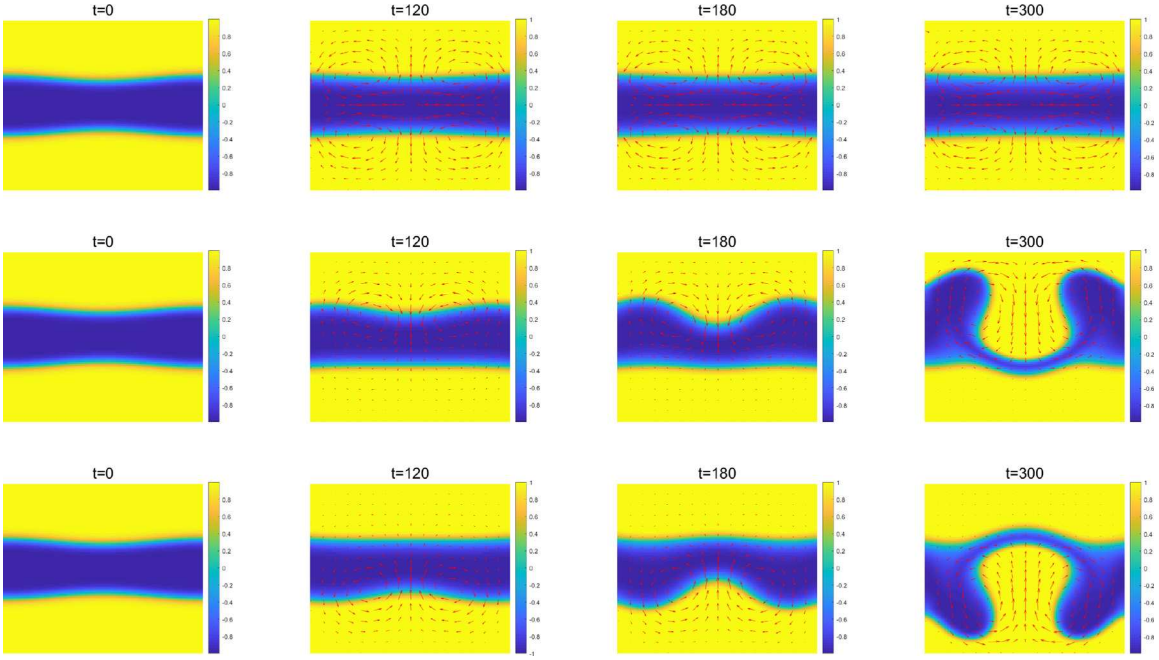

Fig. 5.4. Snapshots of the velocity and phase field obtained from Model 1, 2, 3 with buoyant force term $\mathbf{F}_e$ at $t = 0, 120, 180, 300$, respectively. Row 1: Model 1 with $M_{13} = 0, M_{a,13} = 0$. The shape of the interface does not change noticeably. Row 2: Model 2 with $M_{13} = 10^{-3}, M_{a,13} = 0$. The fluid convection is primarily driven by the thermally induced buoyant force. The interface deformation is mainly because of the thermal induced fluid mixing: the hotter fluid moves up and cooler one comes down. Initially, four small roll cells are present in the vicinity of the interface at $t = 24$. As the temperature gradient in the system persists, roll cell patterns also change gradually. The roll cells correlate to the fluid motion leading to fluid interface deformation. Row 3: Model 3 with $M_{13} = 0, M_{a,13} = 10^{-3}$. Once again, fluid convection is primarily induced by the thermally induced buoyant force. The same physical mechanism as alluded to in Model 2 leads to the shown fluid pattern and temperature distribution. As the temperature distribution is different from Model 2, the pattern of the interface in this model seems to be opposite to that in Model 2.

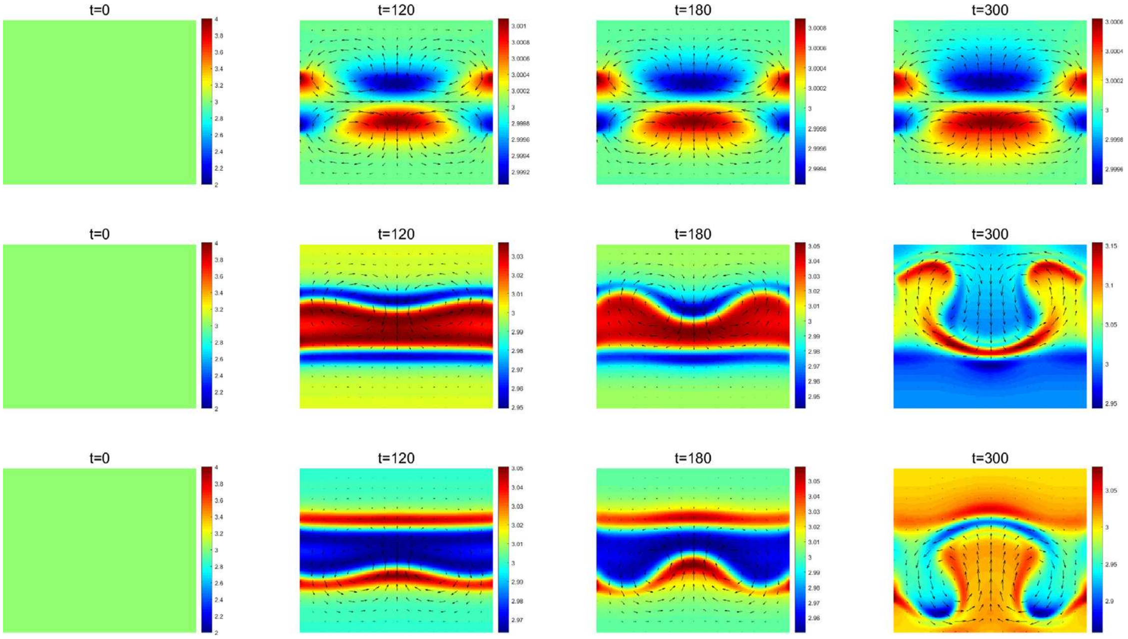

Fig. 5.5. Snapshots of the velocity and temperature field obtained from Model 1, 2, 3 with buoyant force $\mathbf{F}_e$ at $t = 0, 120, 180, 300$, respectively. Row 1: Model 1 with $M_{13} = 0, M_{a,13} = 0$. Row 2: Model 2 with $M_{13} = 10^{-3}, M_{a,13} = 0$. Row 3: Model 3 with $M_{13} = 0, M_{a,13} = 10^{-3}$. The temperature distribution of Model 2 seems to mirror-image that of Model 3.

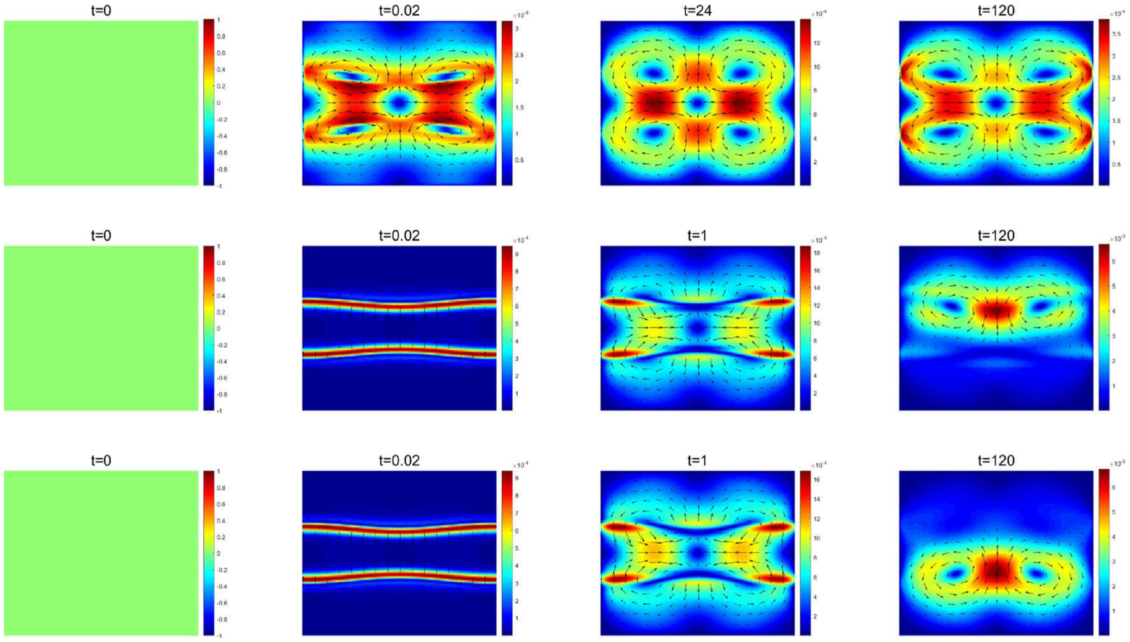

Fig. 5.6. The energy flux of Model 1, 2, 3 with the adiabatic boundary condition at four selected time. Row 1: Model 1 with $M_{13} = 0, M_{a,13} = 0$. Row 2: Model 2 with $M_{13} = 10^{-3}, M_{a,13} = 0$. Row 3: Model 3 with $M_{13} = 0, M_{a,13} = 10^{-3}$. Without cross-coupling, the energy flux is symmetrically distributed vertically. With the entropy enhancing cross-coupling, the higher energy flux region occurs in the top half. Whereas, the energy flux is larger in the bottom part with entropy conservative cross-coupling.

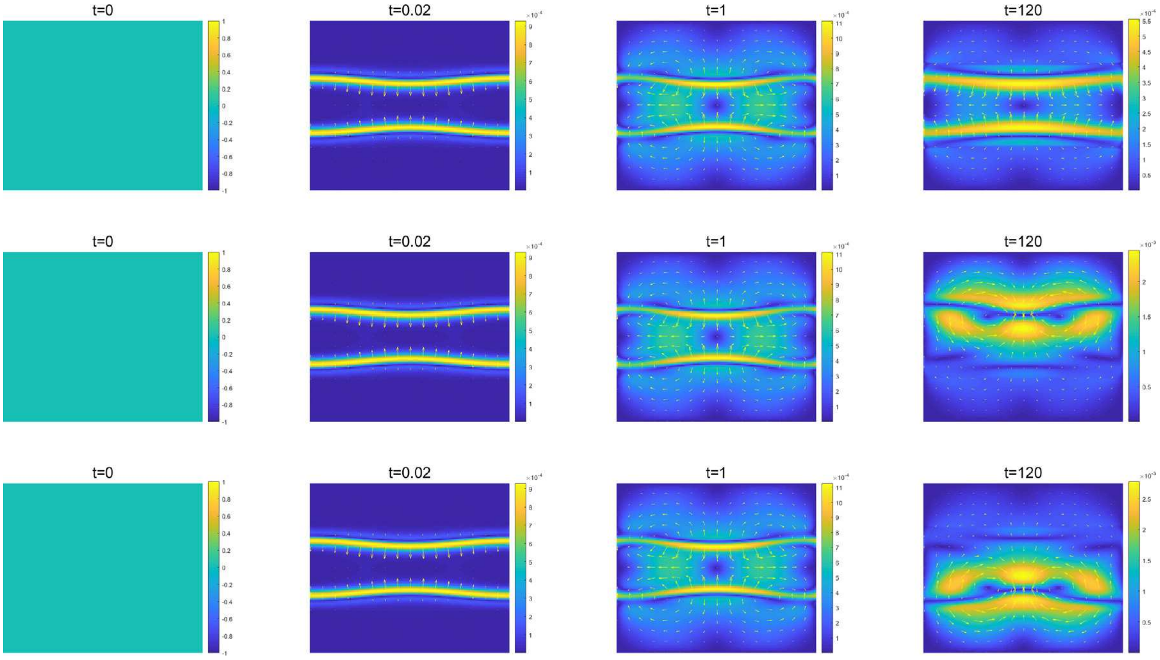

Fig. 5.7. The material flux of Model 1, 2, 3 with the adiabatic boundary condition at four selected time. Row 1: Model 1 with $M_{13} = 0, M_{a,13} = 0$. The material flux of Model 1 exhibits symmetry in the domain. Row 2: Model 2 with $M_{13} = 10^{-3}, M_{a,13} = 0$. Initially, the material flux is nearly symmetric, but later more material transport takes place in the upper half of the domain. Row 3: Model 3 with $M_{13} = 0, M_{a,13} = 10^{-3}$. The materials transport pattern mirror images that of Model 2.

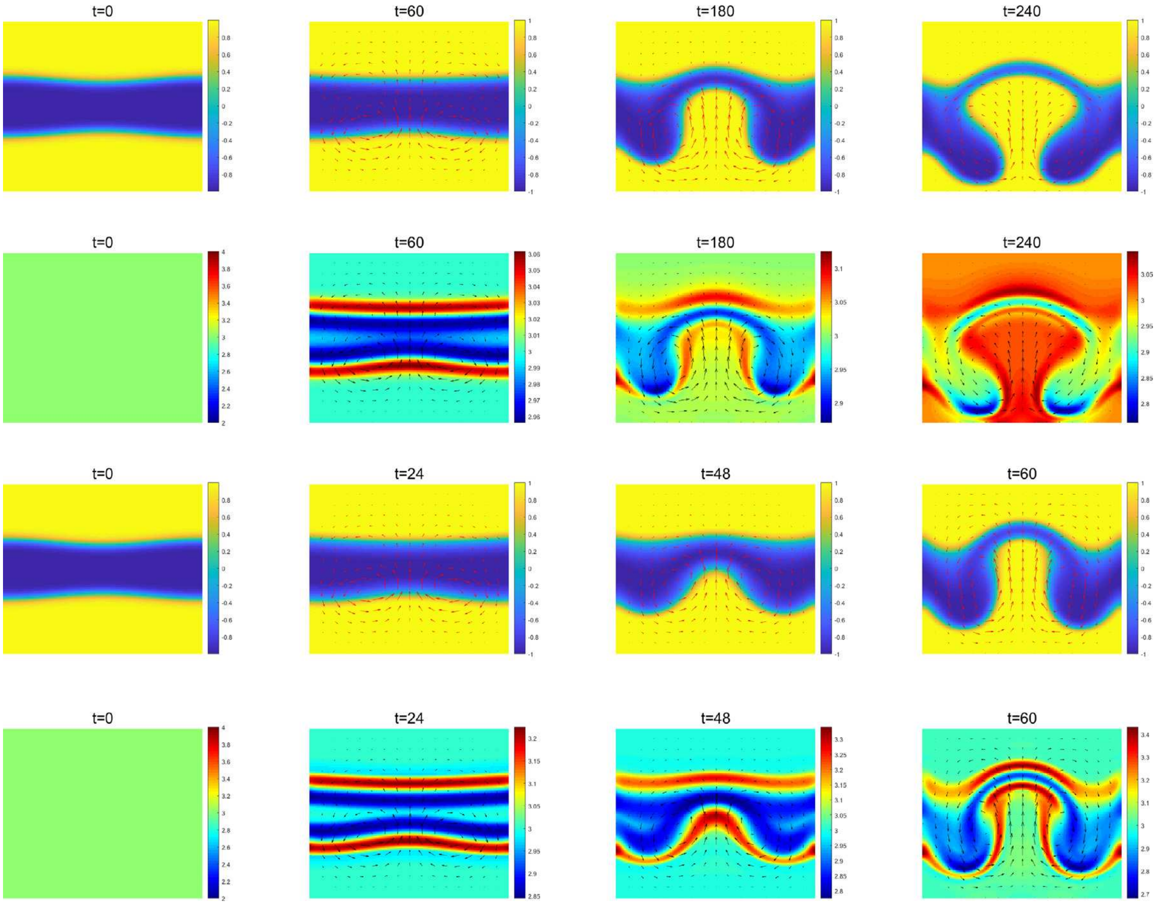

Fig. 5.8. Snapshots of the velocity, phase, and temperature field of Model 4 and Model 3 with the buoyant force at selected times. Row 1: the velocity and phase field of Model 4 with $M_{13} = 10^{-3}$, $M_{a,13} = 2.5 \times 10^{-3}$. Row2: the velocity and temperature field of Model 4. Row 3: the velocity and phase field of Model 3 with $M_{13} = 0$, $M_{a,13} = 10^{-2}$. Row 4: the velocity and temperature field of Model 3.

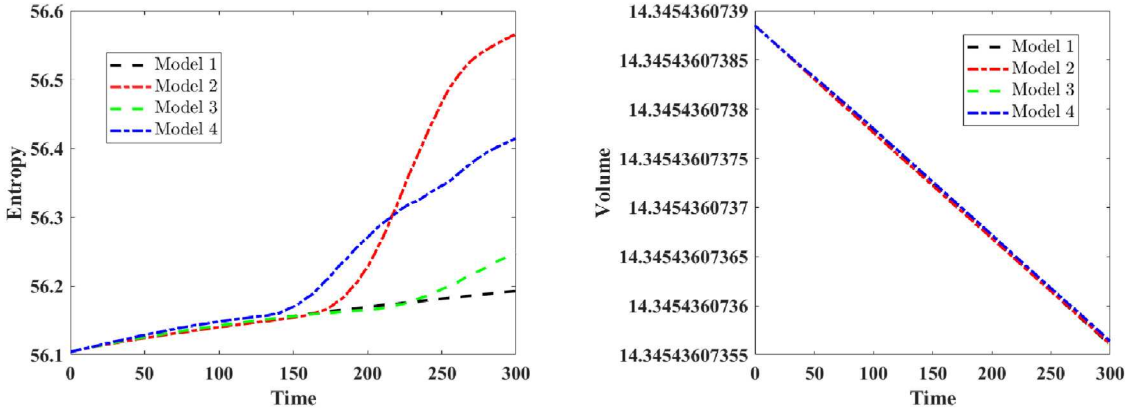

(a) Evolution of entropy S.

(b) Evolution of volume.

Fig. 5.9. Time evolution of the entropy and volume of binary fluid with respect to Model 1, 2,3. (a): Entropy S increases with time. (b): The Volume of fluid 1, which is nearly a constant. These show that the schemes of the three models preserve the positive entropy production rate and the volume of each phase at the discrete level.

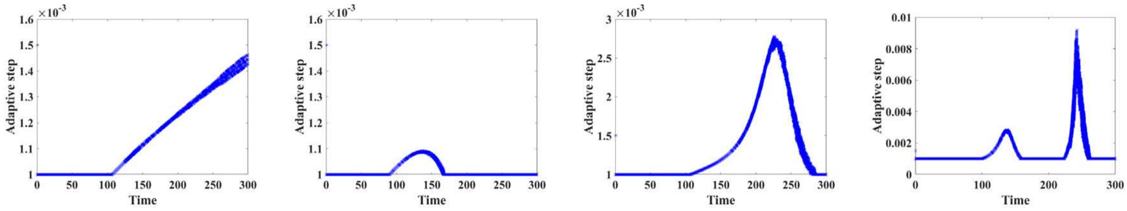

(a) Model 1. (b) Model 2. (c) Model 3. (d) Model 4.

Fig. 5.10. Variations of the adaptive time step over time with respect to Model 1,2,3,4. (a). The adaptive time step of Model 1. (b). The adaptive time step of Model 2. (c). The adaptive time step of Model 3. (d). The adaptive time step of Model 4. These show that the adaptive time-stepping strategy can indeed accelerate the numerical simulation process in the long time simulation while retain the desired accuracy.

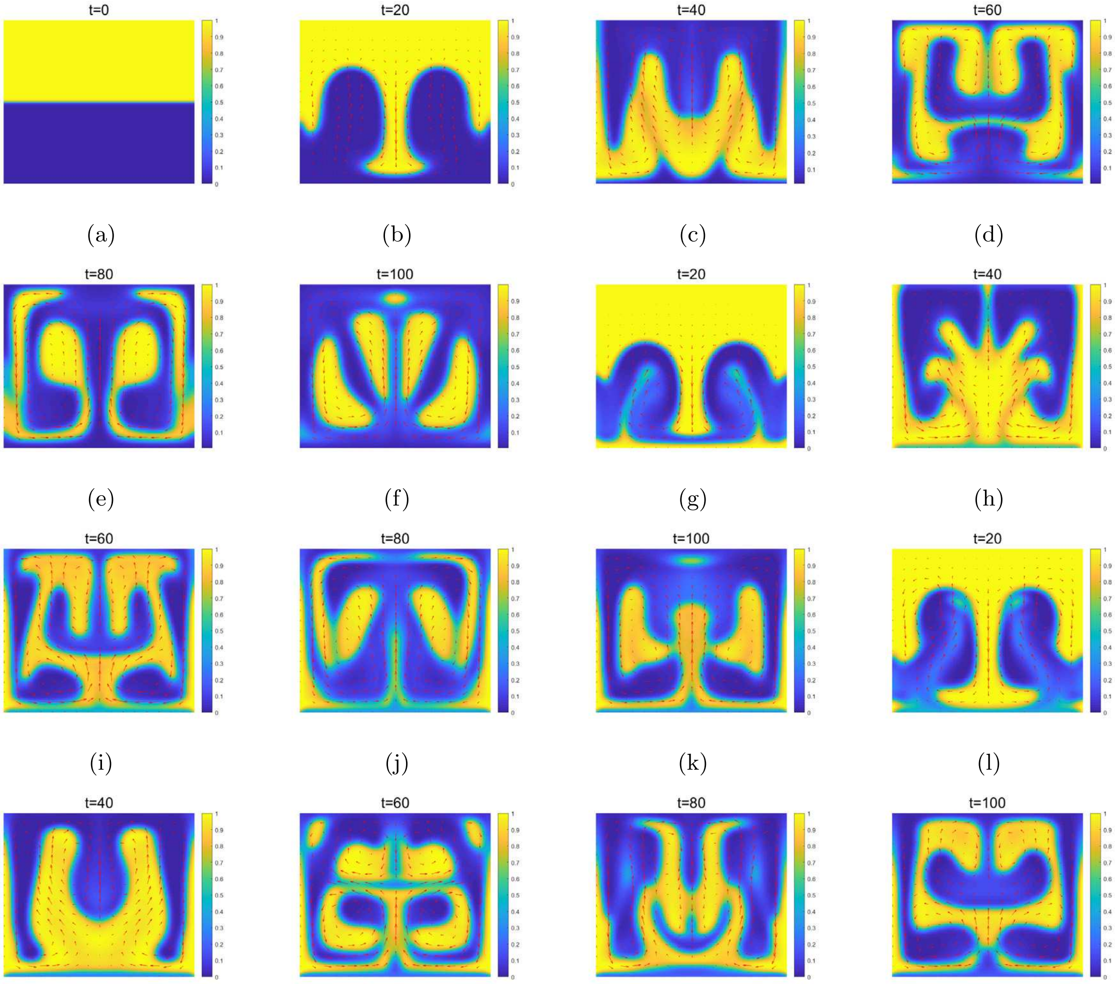

(a) (b) (c) (d)
(e) (f) (g) (h)
(i) (j) (k) (l)
(m) (n) (o) (p)

Fig. 5.11. Snapshots of the velocity and phase field obtained from Model 1, 2, 3 with the non-adiabatic boundary condition at $t = 0, 20, 40, 60, 80, 100$, respectively. The binary fluid is heated from the bottom. (a)–(f): Model 1. The results show that as the binary fluid is heated at the bottom, its density decreases, so the buoyant force pushes the less-dense fluid up towards into the cooler end of the domain. Meanwhile, the cooler fluid at the top becomes denser, so it sinks to displace the warmer fluid due to gravity, a typical scenario of Bernard convection. The interface deformation is led by the thermally induced fluid mixing. (g)–(k): Model 2. The interface deformation is mainly caused by the thermally induced fluid mixing. However, a comparison with the results of Model 1 shows that the mixing effect is significantly enhanced in Model 2 due to the entropy enhancing cross-coupling. (l)–(p): Model 3. The interface deformation is caused by the thermally induced fluid mixing. However, the entropy-preserving cross-coupling seems to retard the fluid mixing in the simulation. For example, the simulation result at $t = 100$ of Model 3 is qualitatively the same as that of Model 1 at $t = 60$. Hence, mixing in Model 3 is weakened compared to Model 1.

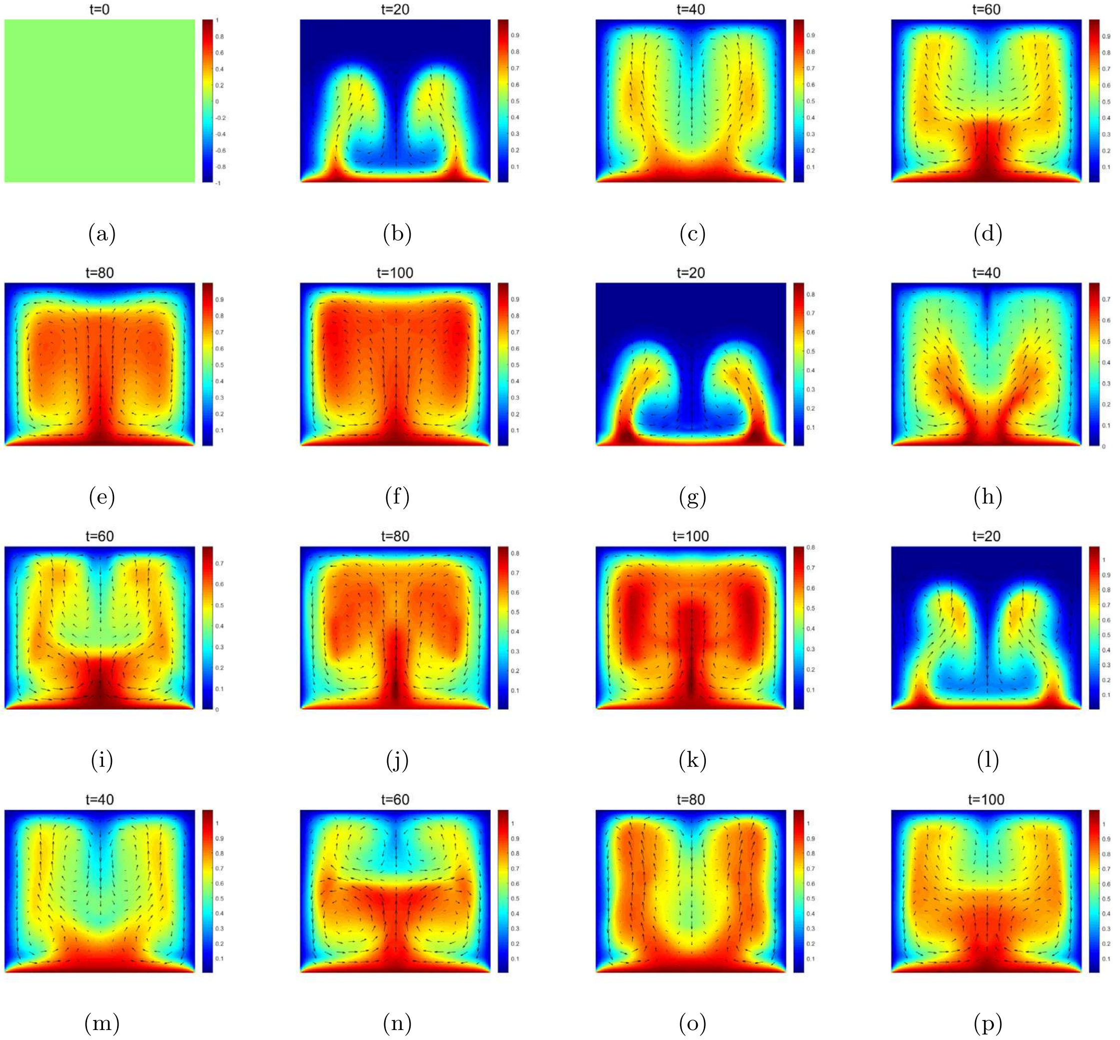

(a) (b) (c) (d)

(e) (f) (g) (h)

(i) (j) (k) (l)

(m) (n) (o) (p)

Fig. 5.12. Snapshots of the temperature and velocity field of Model 1, 2, 3 with the non-adiabatic boundary condition at $t = 0, 20, 40, 60, 80, 100$, respectively. (a)–(f): Model 1. (g)–(k): Model 2. (l)–(p): Model 3. Comparing the three models, we note that the temperature distribution evolves fastest in Model 2 and slowest in Model 3. The observation support the descriptions in the previous figure caption.

References

[1] Clayton TC. Multiphase flow handbook. 2nd ed. Boca Raton: CRC Press; 2005.
[2] Brennen CE. Fundamentals of multiphase flows. Cambridge University Press; 2005.
[3] Anderson MP, Woessner WW, Hunt RJ. Applied groundwater modeling. Elsevier; 2015.
[4] Larson RG. The structure and rheology of complex fluids. 1st ed. Oxford: Oxford University Press; 1998.
[5] DeGroot SR, Mazur P. Nonequilibrium thermodynamics: conservation laws. New York: Dover; 1984.
[6] Tryggvason G, Bunner B, Esmaeeli A, Juric D, Al-Rawahi N, Tauber W, et al. A front-tracking method for the computations of multiphase flow. J Comput Phys 2001;169(2):708–59.
[7] Hirt CW, Nichols BD. Volume of fluid (VOF) method for the dynamics of free boundaries. J Comput Phys 1981;39(1):201–25.
[8] Rajendran S, Manglik RM, Jog MA. New property averaging scheme for volume of fluid method for two-phase flows with large viscosity ratios. J Fluids Eng 2022;144(6):061101.
[9] Mirjalili S, Jain SS, Dodd MS. Interface-capturing methods for two-phase flows: an overview and recent developments. Center for Turbulence Research Annual Research Briefs; 2017, p. 117–38.
[10] Allen SM, Cahn JW. A microscopic theory for antiphase boundary motion and its application to antiphase domain coarsening. Acta Metall 1979;27(6):1085–95.
[11] Cahn JW, Hilliard JE. Free energy of a non-uniform system. i. interfacial free energy. J Chem Phys 1985;28(2):258–67.
[12] Boyer F. Mathematical study of multiphase flow under shear through order parameter formulation. Asymptot Anal 1999;20(2):175–212.
[13] Chen LQ. Phase-field models for microstructure evolution. Annu Rev Mater Res 2002;32:113–40.
[14] Morton EG, Debra AP, Jorge V. Two-phase binary fluids and immiscible fluids described by an order parameter. Math Methods Appl Sci 1996;6:815–31.
[15] Kapustina M, Tsygankov D, Zhao J, Wessler T, Yang X, Chen A, et al. Modeling the excess cell surface stored in a complex morphology of bleb-like protrusions. PLoS Comput Biol 2016;12(3):1004841.
[16] Bechtel SE, Forest MG, Rooney F, Wang Q. Investigation of simplified thermal expansion models compressible Newtonian fluids applied to nonisothermal plane Couette and Poisuille flows. Phys Fluids 2004;16(11):3955–74.
[17] Bechtel SE, Rooney F, Wang Q. A thermodynamic definition of pressure for incompressible viscous fluids. Internat J Engrg Sci 2004;42(19–20):1987–94.
[18] Gong YZ, Zhao J, Wang Q. Linear second-order in time energy stable schemes for hydrodynamic models of binary mixtures based on a spatially pseudospectral approximation. Adv Comput Math 2016;44(5):1573–600.
[19] Zhang T, Wang Q. Cahn–Hilliard vs singular Cahn–Hilliard equations in phase field modeling. Commun Comput Phys 2010;7(2):362–74.

[20] Li J, Wang Q. A class of conservative phase field models for multiphase fluid flows. J Appl Mech 2014;81(2):021004.
[21] Zhao J, Wang Q. Three-dimensional numerical simulations of biofilm dynamics with quorum sensing in a flow cell. Bull Math Biol 2017;79(5):884–919.
[22] Chen C, Ren M, Srinivasan A, Wang Q. 3-D simulations of biofilm-solvent interaction. East Asian J Appl Math 2011;1(2):197–214.
[23] Bertei A, Tellini B, Mauri R. Dynamic transition of dendrite orientation in the diffusive spinodal decomposition of binary mixtures under a thermal gradient. Chem Eng Sci 2019;203:450–63.
[24] Pecenko A. Non-isothermal two-phase flow with a diffuse-interface model. Int J Multiphas Flow 2011;37(2):149–65.
[25] Li J, Zhao J, Wang Q. Energy and entropy preserving numerical approximations of thermodynamically consistent crystal growth models. J Comput Phys 2019;382:202–20.
[26] Guo ZL, Lin P. A thermodynamically consistent phase-field model for two-phase flows with thermocapillary effects. J Fluid Mech 2015;766:226–71.
[27] Sun SW, Wang Q. Entropy-production-rate-preserving algorithms for a hydrodynamical model of binary fluids. J Sci Comput 2024;101:53.
[28] Abbasi FM, Iqbal J, Nawaz R. Analysis of thermal characteristics for MHD peristaltic movement of hybrid nanofluid with electro-osmosis, Ohmic heating and Hall effects. Int J Heat Fluid Flow 2024;107:109405.
[29] Iqbal J, Abbasi FM, Alkinidri M, Alahmadi H. Heat and mass transfer analysis for MHD bioconvection peristaltic motion of Powell–Eyring nanofluid with variable thermal characteristics. Stud Therm Eng 2023;43:102692.
[30] Iqbal J, Abbasi FM, Ali I. Heat transfer analysis for magnetohydrodynamic peristalsis of Reiner–Philippoff fluid: Application of an artificial neural network. Phys Fluids 2024;36(4):041914.
[31] Chen Long-Qing. Phase-field method of phase transitions/domain structures in ferroelectric thin films: A review. J Am Ceram Soc 2008;91(6):1835–44.
[32] Indergand Roman, Vidyasagar A, Nadkarni Neel, Kochmann Dennis M. A phase-field approach to studying the temperature-dependent ferroelectric response of bulk polycrystalline PZT. J Mech Phys Solids 2020;144:104098.
[33] Byron B, Robert CA, Ole H. Dynamics of polymeric liquids: fluid mechanics. Vol. 1. 2nd ed. New York: John Wiley & Sons; 1987.
[34] Byron B, Charles FC, Robert CA, Ole H. Dynamics of polymeric liquids: fluid mechanics. Vol. 2. 2nd ed. New York: John Wiley & Sons; 1987.
[35] Wang Q. Frontiers and progress of current soft matter research: dynamics of polymeric liquids-i fluid mechanics. Singapore: Springer Singapore; 2021.
[36] Shen J, Xu J, Yang J. The scalar auxiliary variable (SAV) approach for gradient flows. J Comput Phys 2018;353:407–16.
[37] Shen J, Xu J, Yang J. A new class of efficient and robust energy stable schemes for gradient flows. SIAM Rev 2019;61:474–506.
[38] Cheng Q, Liu C, Shen J. A new Lagrange multiplier approach for gradient flows. Comput Methods Appl Mech Engrg 2020;367:113070.
[39] Sun SW, Li J, Zhao J, Wang Q. Structure-preserving numerical approximations to a non-isothermal hydrodynamic model of binary fluid flows. J Sci Comput 2020;83:3.
[40] Zhao J, Wang Q, Yang XF. Numerical approximations to a new phase field model for two phase flows of complex fluids comput methods. Appl Mech Eng 2016;310:77–97.
[41] Zhao J, Yang XF, Gong YZ, Zhao XP, Yang XG, Li J, et al. A general strategy for numerical approximations of non-equilibrium models part i: thermodynamical systems. Int J Numer 2018;15(6):884–918.
[42] Gong YZ, Zhao J, Wang Q. Linear second order in time energy stable schemes for hydrodynamic models of binary mixtures based on a spatially pseudospectral approximation. Adv Comput Math 2018;44:1573–600.
[43] Velzen DV, Cardozo RL. Langenkamp h: A liquid viscosity-temperature-chemical constitution relation for organic compounds. Ind Eng Chem Fund 1972;11(1):20–5.
[44] Jing XB, Wang Q. Thermodynamically consistent models for coupled bulk and surface dynamics. Entropy 2022;24(11):1683.
[45] Jing XB, Wang Q. Thermodynamically consistent dynamical boundary conditions of phase field models. Commun Math Sci 2023;21:3.
[46] Li J, Zhao J, Wang Q. Energy and entropy preserving numerical approximations of thermodynamically consistent crystal growth models. J Comput Phys 2019;382:202–20.